

METAL SUBSTITUTION WITHIN NANOSTRUCTURED NICKEL HYDROXIDES
FOR AQUEOUS RECHARGEABLE
NICKEL-ZINC BATTERIES

by

Samuel W. Kimmel, A.A., A.S., B.S.

A thesis submitted to the Graduate Council of
Texas State University in partial fulfillment
of the requirements for the degree of
Master of Science
with a Major in Chemistry
August 2020

Committee Members:

Christopher P. Rhodes, Chair

Gary Beall

Benjamin Martin

COPYRIGHT

by

Samuel W. Kimmel

2020

FAIR USE AND AUTHOR'S PERMISSION STATEMENT

Fair Use

This work is protected by the Copyright Laws of the United States (Public Law 94-553, section 107). Consistent with fair use as defined in the Copyright Laws, brief quotations from this material are allowed with proper acknowledgement. Use of this material for financial gain without the author's express written permission is not allowed.

Duplication Permission

As the copyright holder of this work I, Samuel W. Kimmel, authorize duplication of this work, in whole or in part, for educational or scholarly purposes only.

DEDICATION

“Sir,” said Stephan, ‘I read novels with the utmost pertinacity. I look upon them—I look upon good novels—as a very valuable part of literature, conveying more exactly and finely distinguished knowledge of the human heart and mind than almost any other, with greater breadth and depth and fewer constraints.’ Patrick O’Brian, *The Nutmeg of Consolation*.

May this work serve as a valuable piece of literature worthy of the greatest fictional ‘natural philosopher’ S. Maturin, who kept me grounded and engaged in the wonders of the natural world when others doubted the likelihood of my success in high school.

ACKNOWLEDGEMENTS

The author would like to acknowledge and thank the staff scientists and post-doctoral researchers at the Code 6170, Surface Chemistry Branch, U.S. Naval Research Laboratory, Washington D.C.: Dr. Debra R. Rolison (Section Head), Dr. Jesse S. Ko, Dr. Ryan H. DeBlock, Dr. Christopher N. Chervin, Dr. Joseph Parker, Dr. Brandon J. Hopkins, and Dr. Jeffrey W. Long for their help and tutelage with the nuances of aqueous nickel-zinc electrochemistry during my multiple summer internships. Thanks are due to the graduate and post-doctoral researchers' students of the Advanced Energy Materials Research Group at Texas State University San Marcos, Texas for their guidance cooperation and patience; specifically, Dr. Fernando Godinez-Salomon, Dr. Sibio Niu, and Luis Albiter. Thank you to all committee members, Dr. Gary Beall, Dr. Benjamin Martin and Dr. Christopher Rhodes, who through their committed support made this work successful. The author gratefully acknowledges support from the Office of Naval Research (Navy Undersea Research Program Grant No. N00014-19-1-2526) and the Naval Research Enterprise Internship Program (NREIP).

TABLE OF CONTENTS

	Page
ACKNOWLEDGEMENTS.....	v
LIST OF TABLES.....	viii
LIST OF FIGURES.....	ix
ABSTRACT.....	x
CHAPTER	
1. INTRODUCTION.....	1
1.1. Unlocking a Sustainable Future with clean energy.....	1
1.2. Nickel-Zinc Alkaline Battery Chemistry.....	3
1.3. Nickel-based Cathodes for Alkaline Batteries.....	5
1.4. Synthesis of α -Ni(OH) ₂	8
1.5. General Principles of Microwave Chemistry.....	11
1.6. Project Motivation and Objectives.....	12
2. EXPERIMENTAL.....	14
2.1. Microwave Synthesis of Ni(OH) ₂ Nanosheets.....	14
2.2. Materials Characterization.....	16
2.3. Electrochemical Characterization.....	17
2.3.1. Electrode Fabrication.....	17
2.3.2. Electrochemical Characterization.....	18
3. RESULTS AND DISCUSSION.....	20
3.1. Analysis of Morphology and Porosity.....	20

3.2. Analysis of Composition	24
3.3 X-ray Diffraction Characterization	25
3.4. Raman Spectroscopic Characterization	27
3.5. Electrochemical Characterization	36
3.5.1. Analysis of 1 st Cycle Galvanostatic Charge-Discharge	36
3.5.2. Analysis of the Effect of Cycling.....	43
4. CONCLUSIONS	48
REFERENCES	50

LIST OF TABLES

Table	Page
1. Nitrogen Porosimetry of metal substituted nanosheets.....	22
2. Elemental analysis of unsubstituted and metal-substituted nanosheets detected by inductively coupled plasma optical emission spectral (ICP-OES) analysis of Ni:M ratio of metal substituted nanosheets.	24
3. Interlayer crystallographic peak position and interlayer spacing of microwave synthesized nanosheets determined from X-ray diffraction.	27
4. Experimental and reported literature values of Raman peak assignments of unsubstituted microwave-synthesized α -Ni(OH) ₂ nanosheet within the 50 cm ⁻¹ to 4000 cm ⁻¹ region.	30
5. Raman peak assignments of unsubstituted and substituted microwave synthesized α -Ni(OH) ₂ nanosheet.....	36
6. Differential capacity analysis of cathodic voltages, anodic voltages and oxygen evolution reaction (OER) of unsubstituted α -Ni(OH) ₂ and substituted nanosheets.	42
7. Electrochemical properties of unsubstituted α -Ni(OH) ₂ and substituted nanosheets	45

LIST OF FIGURES

Figures	Page
1. Safety related issues inherent with the use of Li-ion batteries.....	2
2. General schematic of an alkaline battery.....	3
3. Schematic of components of Ni–Zn rechargeable battery	5
4. Relating the electrochemical performance to the crystal structure	7
5. Various Ni(OH) ₂ synthetic routes.....	9
6. Principles of microwave heating.....	11
7. Images of ~25mg of each microwave synthesized nanosheets powder.....	15
8. Schematic representation of laser cut-gas tight- acrylic battery cells.....	18
9. Scanning electron micrographs of microwave synthesized nanosheets	21
10. Barrett–Joyner–Halenda desorption pore distribution plots	23
11. X-ray diffraction spectra of microwave synthesized nanosheets.....	26
12. Raman spectra of unsubstituted α -Ni(OH) ₂ with peak assignments.....	29
13. Raman spectrum of substituted α -Ni(OH) ₂	32
14. First cycle discharge capacity	38
15. First cycle differential capacity (dQ/dV) analysis	41
16. Effect of cycling on the discharge capacity	44
17. Effect of cycling on the differential capacity (dQ/dV).....	46

ABSTRACT

Developing batteries with high gravimetric and volumetric energy density, improved safety, and lower cost is a critical need for a wide range of applications including electric vehicles, portable electronic devices, and grid-level energy storage. Although lithium-ion is currently the go-to high-energy battery technology, the inherent safety issues of Li-ion persist and represent a challenge for large-format applications. The alkaline nickel–zinc (Ni–Zn) battery is an attractive alternative to Li-ion due to its use of nonflammable aqueous electrolyte. The monolithic three-dimensional zinc “sponge” developed at the U.S. Naval Research Laboratory solves long-standing performance limitations for zinc anodes and paves the way for next generation Ni–Zn batteries that approach the specific energy of Li-ion systems. To match these new levels of zinc anode function in terms of capacity and rate capability, improved alkaline cathode materials and architectures are required. To meet this need, the effect of isomorphous substitution of metal ions (aluminum, cobalt, manganese and zinc) into α -Ni(OH)₂ by microwave synthesis was investigated because α -Ni(OH)₂ can accommodate more than one-electron charge storage when stabilized, which otherwise converts to lower-capacity β -Ni(OH)₂ with cycling in alkaline electrolytes. A rapid and scalable microwave-assisted route was used to synthesize substituted α -Ni(OH)₂ with a nanosheet morphology. The effect of metal-ion substituents on the structure and morphology of α -Ni(OH)₂ was determined using scanning electron microscopy, X-ray diffraction, nitrogen porosimetry and Raman spectroscopy. Electrochemical charge–storage behavior was evaluated using

galvanostatic cycling and differential-capacity measurements under device-relevant conditions. The results show that when α -Ni(OH)₂ is synthesized by a microwave-assisted hydrothermal route with a partial substitution at a Ni²⁺-to- M^{z+} ratio of 9:1 (nominally Ni_{0.9}M_{0.1}), the identity of the metal substituent influences the relative concentration of Ni²⁺-to- M^{z+} incorporated into the α -Ni(OH)₂ nanosheets. Manganese incorporated less (Ni_{0.98}Mn_{0.02}) than the nominal substitution ratio while zinc was incorporated to a greater degree (Ni_{0.81}Zn_{0.19}). The identity of a metal substituent also influenced physicochemical and electrochemical properties of microwave synthesized α -Ni(OH)₂ nanosheets. Raman spectroscopy indicated the incorporation of ethylene glycol, urea, and two different nitrate environments, and the x-ray diffraction pattern supported the α -phase crystal structure was maintained upon substitution. Specific substituents increased (Co and Zn) or decreased (Al) the aggregate size of the nanosheets while still preserving the mesoporous and microporous structure. Compared with the initial electrochemical discharge capacity of unsubstituted α -Ni(OH)₂ nanosheets of 239 mAh g⁻¹_{active}, Al³⁺ substitution increased the capacity from to 303 mAh g⁻¹_{active}, whereas Co²⁺ substitution decreased the capacity to 189 mAh g⁻¹_{active}. Understanding the nature of metal substituents within the α -Ni(OH)₂ structure and the resulting effect on the charge storage process furthers the development of energy dense Ni–Zn batteries.

1. INTRODUCTION

1.1. Unlocking a Sustainable Future with clean energy

Transitioning to renewable energy from a historically fossil fuel-based consumption model has become increasingly popular. Unfortunately, the conversion is significantly hindered by inability to efficiently store harvested energy. There are two main factors that limit integrating renewable energy into the power grid: (i) local conditions can alter the amount of energy harvested, and (ii) conventional power grid systems cannot effectively incorporate the energy into the grid, both of which can add instability to the power supply.¹

Lithium ion (Li-ion) batteries have been incentivized since 2011 as a way of reducing greenhouse gas emissions and increasing energy independence.² In 2012, electric vehicle sales accounted for 0.1% of vehicles sold in the United States attributed to the high cost (\$30,000 for 240 mile range) and low energy density (400-800 kW⁻¹) of rechargeable Li-ion batteries.² Recently companies like Tesla and Chevrolet have reduced cost and improved the energy capacity, and the International Energy Agency expects the number of Li-ion powered electric vehicles to surpass 100 million by 2025, consequently bringing the crash rate of electric vehicles to near the levels of gasoline-powered vehicles.³

As the number of electric vehicles increases, so should the safety concerns associated with Li-ion batteries. Boeing encountered similar safety issues on their 787 Dreamliner aircraft (Figure 1a)⁴ while Samsung (Figure 1b)⁵ was forced to issue a recall of their Galaxy Note cell phones. In both cases devices powered with Li-ion batteries caught fire resulting the European union to ban all Li-ion batteries on aeroplanes.⁶ If a Li-ion battery

pack is split open, a battery thermal runaway event could be triggered causing an explosion and fire as seen when a Tesla Model S (Figure 1c) caught fire after colliding with road debris.^{3, 7}



Figure 1. Safety related issues inherent with the use of Li-ion batteries. A) Grounding of the 787 Dreamliner due to battery fire risks,⁴ B) Recall of Samsung Note 7,⁵ C) Collisional induced fires in Tesla Model S.⁷

A more sustainable future requires developing batteries with high gravimetric and volumetric energy density, improved safety, and lower cost in order to ensure wider implementation of electric vehicles, decentralized energy storage, and grid-level energy storage, while increasing time between recharging portable electronic devices. Although lithium-ion is currently the go-to high-energy battery technology, the inherent safety issues of Li-ion persist and represent a continued challenge, particularly for large-format applications such as electric vehicle battery packs, which contain three orders of magnitude more energy than a laptop battery pack.⁸

One of the chief safety concerns with Li-ion batteries is the use of flammable electrolytes. Nickel-zinc batteries offer an attractive alternative to Li-ion due to their nonflammable aqueous electrolytes.

1.2. Nickel-Zinc Alkaline Battery Chemistry

The general schematic (Figure 2)⁹ of an alkaline battery can be used to conceptualize the electrochemical reaction of a rechargeable battery discussed below. Common electrode materials used in the majority alkaline batteries are derived from zinc, manganese, nickel or cobalt.⁹ A popular nickel based alkaline battery, the Nickel-Zinc (Ni-Zn) battery, uses nickel hydroxide; $\text{Ni}(\text{OH})_2$, as the cathode and zinc/zinc oxide as the anode material.¹⁰ This alternative to lithium-ion couples high energy and power densities with a high open circuit potential (1.75V) and a theoretical energy density of 372 Wh kg^{-1} .⁹

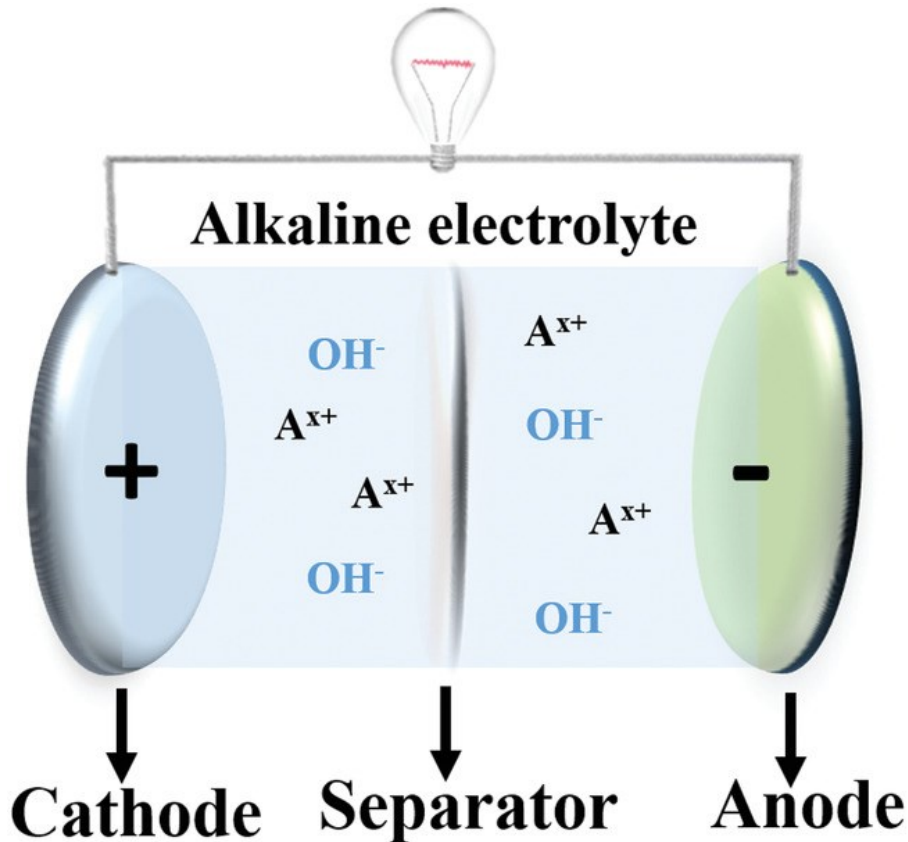
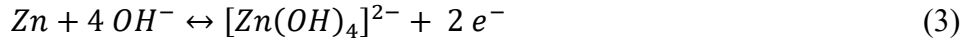
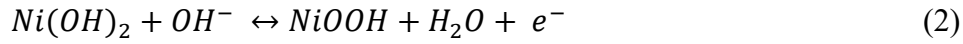


Figure 2. General schematic of an alkaline battery.⁹

The overall electrochemical equation for an aqueous alkaline Ni-Zn battery cell is given by equation 1⁹, the cathodic half-cell is given by equation 2⁹, and the anodic half-cell is given by equation 3⁹:



When the Ni-Zn electrochemical cell is discharged, nickel oxyhydroxide (NiOOH), is reduced to Ni(OH)₂ and zinc metal is oxidized to zinc oxide/hydroxide. The electrochemistry of the zinc anode half-cell (equation 3) in an alkaline solution is more nuanced;^{6, 9, 10} however, its complete mechanism is outside the scope of this work which involves studying the cathode. If the Ni-Zn cell is overaged several parasitic reactions occur, which include oxygen forming at the cathode and hydrogen at the anode.¹⁰

A “monolithic three-dimensional (3D) zinc sponge” anode (Figure 3) was developed at the U.S. Naval Research Laboratory (NRL), and the zinc sponge anode overcomes long-standing cycling performance limitations of zinc anodes providing a potential anode for next generation Ni-Zn batteries that can be competitive with the specific energy of Li-ion systems.⁶ Rewiring the zinc anode as porous 3D monolith enables more uniform charge/discharge at greater zinc utilization while preventing dendritic growth at the zinc anode.

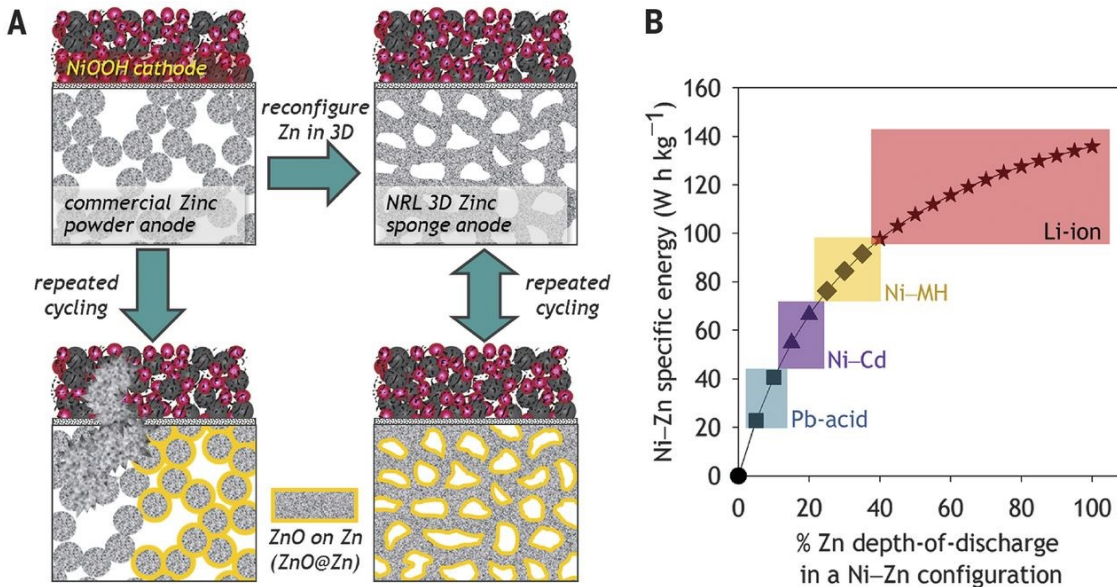


Figure 3. Schematic of components of Ni-Zn rechargeable battery. A) Schematic of components of Ni-Zn rechargeable battery with NRL's Zn sponge anode and Ni(OH)₂ cathode. B) The calculated specific energy of a fully packaged Ni-Zn cell as a function of increasing Zn depth of discharge versus a capacity matched Ni(OH)₂ electrode. Shaded areas highlight the specific energy range of common battery chemistries: e.g., at $\geq 40\%$ DOD_{Zn} (percentage of theoretical utilization), Ni-Zn becomes competitive with Li-ion even at the single-cell level.⁶

This redesign has reopened the door for zinc-based battery chemistries that can approach the system-level energy density of lithium ion, without the accompanying deadweight wasted space required to mitigate system-failures. Several iterations of the Zn “sponge” anode have continued to improve the electrochemical performance, scalability, mechanical durability, and have been shown to outpace not one, but four commercially harvested nickel hydroxide cathodes per anode.^{6, 11-14} To match these new levels of zinc anode function in terms of capacity and rate capability requires improving alkaline cathode materials and architectures.

1.3. Nickel-based Cathodes for Alkaline Batteries

Nickel hydroxide has been used as a battery component since the early 1950's with the reversible electrochemical oxidation/reduction of nickel (II) hydroxide \leftrightarrow nickel (III) oxyhydroxide (Figure 4a).¹⁵ This reaction scheme involves two oxidized phases (β -

NiOOH and γ -NiOOH) and two reduced phases (β -Ni(OH)₂ and α -Ni(OH)₂).¹⁵

The two pseudo-polymorphs of Ni(OH)₂ are β -Ni(OH)₂ (Figure 4b) and α -Ni(OH)₂ (Figure 4a).¹⁵ β -Ni(OH)₂ is isostructural to brucite, whereas α -Ni(OH)₂ is made up of layers of β -Ni(OH)₂ intercalated with anions and water molecules.¹⁵ The intercalated molecules do not occupy a particular crystallographic site within the structure but have some rotational and translational freedom thereby acting as “an amorphous glue” forming hydrogen bonding between the β -Ni(OH)₂ layers creating a turbostratic structure.^{15, 16}

Commercial Ni–Zn batteries use β -Ni(OH)₂ cathodes that have a practical capacity of $\sim 263 \text{ mAh g}^{-1}$ at a C-rate (current rate expressed as a multiplier of a stated capacity in ampere-hours¹⁰) of 0.2C,¹⁷ (capturing 90% of the theoretical one-electron (Ni^{2+/3+}) capacity of 289 mAh g^{-1}). Additional challenges inherent to β -Ni(OH)₂ are: (i) a steep drop in capacity at high rates, and (ii) overcharging generates γ -NiOOH causing large volumetric changes that result in battery failure.¹⁸ Compared to β -Ni(OH)₂, α -Ni(OH)₂ has a higher theoretical capacity ($\sim 487 \text{ mAh g}^{-1}$) derived from storing ~ 1.67 electrons per Ni and partially poisoning Ni as Ni⁴⁺,¹⁹ yet α -Ni(OH)₂ is unstable at high pH, converting to the lower-capacity β -Ni(OH)₂ phase in alkaline electrolytes.²⁰

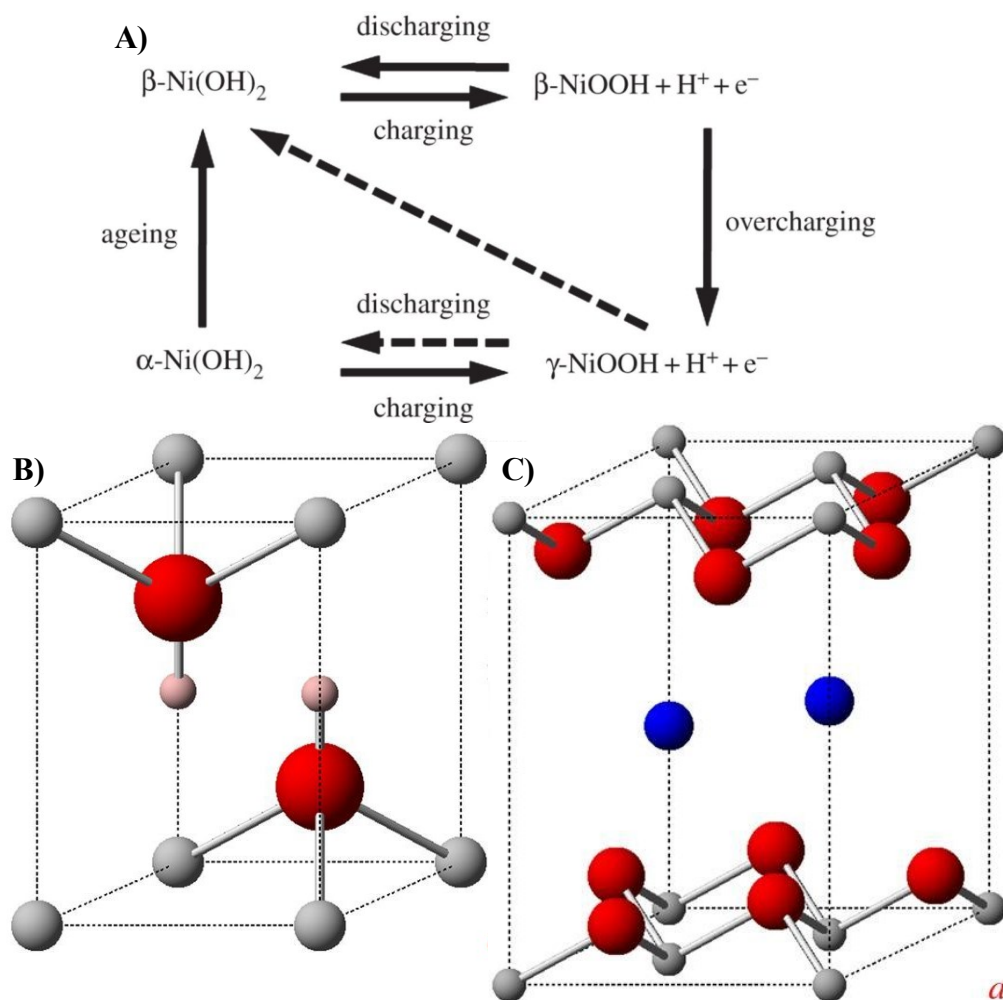


Figure 4. Relating the electrochemical performance to the crystal structure. A) Electrochemical relationship between the different polymorphs of Ni(OH)₂; B) crystal Structure of β-Ni(OH)₂; C) crystal Structure of α-Ni(OH)₂.¹⁵

Metal substituents can influence the physical and electrochemical performance of α-Ni(OH)₂ cathodes. Prior studies have investigated such cation substituents as aluminum^{17, 21-28}, cobalt^{24, 25, 29-31}, copper^{31, 32}, chromium^{31, 33}, iron³¹, manganese^{31, 33, 34}, tin³¹ and zinc^{31, 35, 36} which appear to influence the stability and charge storage of α-Ni(OH)₂.

Ethylene glycol has also been reported to stabilize the α-phase.³⁷

In addition to the capacity of the cathode, redox potentials are an important consideration when operating within an aqueous alkaline electrolyte because Ni(OH)₂ electrocatalyzes the oxygen-evolution reaction (OER). The OER parasitic reaction occurs

near the Ni(OH)₂/NiOOH redox potential, decreases charge efficiency, and lowers discharge capacity.¹⁸ Coprecipitation with a variety of metals has been shown to influence the Ni^{2+/3+} redox potential and either catalyze or poison the oxygen evolution reaction that occurs near the nickel redox.³¹

1.4. Synthesis of α -Ni(OH)₂

The synthetic route to Ni(OH)₂ plays a significant role in the resulting crystal structure, morphology, structure, and electrochemical properties.¹⁵ There are six common routes to synthesis of Ni(OH)₂ (Figure 5) briefly described by the following: chemical precipitation (Figure 5a), electrochemical precipitation (Figure 5b), sol-gel synthesis (Figure 5c), chemical aging (Figure 5d), hydrothermal/solvothermal synthesis (Figure 5e), and surface layering on a nickel alloy (Figure 5f).¹⁵

Chemical precipitation (Figure 5a) is a one pot synthesis where a basic solution is added dropwise to a solution of nickel (II) salt. The phase and crystallinity of the precipitate are determined by the temperature, concentrations and identities of both the nickel (II) salt and the basic solution used with room temperature reaction conditions forming α -Ni(OH)₂ while higher temperatures result in forming a mixed α/β - Ni(OH)₂ material.¹⁵

Electrochemical precipitation (Figure 5b) deposits a thin layer of either α -Ni(OH)₂, a mixed α/β Ni(OH)₂, or β -Ni(OH)₂ onto a conductive substrate by placing the substrate into a solution of nickel (II) salt held at a negative potential.¹⁵ Similar to chemical precipitation, the phase and crystallinity of the product depends on the nickel (II) salt concentration/identity and current density.¹⁵ Generally, current densities of $\sim 0.5 \text{ mA cm}^{-2}$ produced α -Ni(OH)₂, while increasing the current density produces α/β -Ni(OH)₂ mixed

phased materials.¹⁵

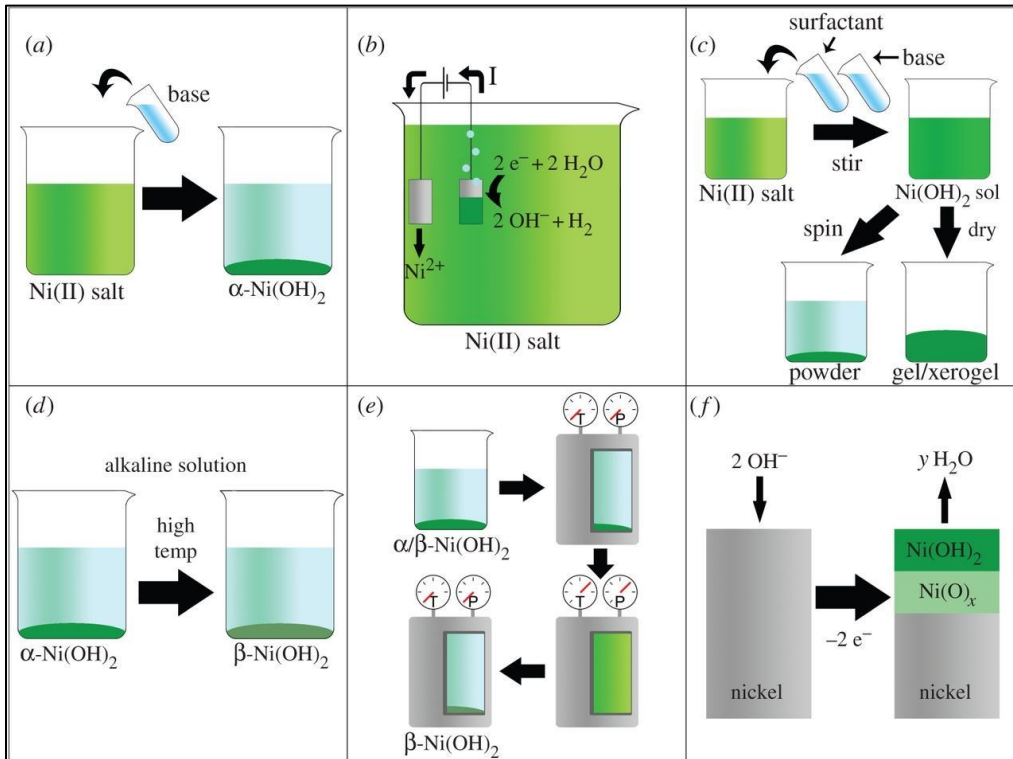


Figure 5. Various $\text{Ni}(\text{OH})_2$ synthetic routes. A) Chemical precipitation, B) Electrochemical precipitation, C) Sol-gel synthesis, D) Chemical aging, E) Hydrothermal Synthesis, and F) Formation of $\text{Ni}(\text{OH})_2$ onto nickel alloys.¹⁵

Sol-gel synthesis (Figure 5c) is the synthetic process of turning a solution into a gel and can be used to prepare both $\alpha\text{-Ni}(\text{OH})_2$ or $\beta\text{-Ni}(\text{OH})_2$ with a variety of porosities and densities.¹⁵ Chemical aging (Figure 5d) purposefully induces the otherwise spontaneous dehydration of $\alpha\text{-Ni}(\text{OH})_2$ into $\beta\text{-Ni}(\text{OH})_2$ in a concentrated alkaline environment at elevated temperatures.¹⁵

Hydrothermal synthesis (Figure 5e) involves an aqueous-based solution and precursor nickel (II) salt heated in a pressure reaction vial allowing the reaction to proceed at higher temperatures than ordinarily allowed under ambient pressure.¹⁵ These reaction conditions typically favor $\beta\text{-Ni}(\text{OH})_2$, but $\alpha\text{-Ni}(\text{OH})_2$ can be synthesized by using: (i) an intercalation agent, (ii) a non-aqueous solution (solvothermal synthesis), (iii) lowering the reaction

conditions, or (iv) including urea in the reaction resulting in ammonia-intercalated α -Ni(OH)₂.¹⁵

Prior work indicated that the anion that accompanies the Ni and Al precursors during synthesis affects interlayer distance and influences electrochemical performance.²⁶ Metal nitrates salts are inexpensive precursors with the potential for large scale solution production of electronic materials.³⁸ With a high solubility in aqueous or polar organic solvents, hydrated metal nitrates salts form complex solution equilibria. For example when nickel nitrate is dissolved in an aqueous solution, the positively charged Ni²⁺ and partial negative charge from H₂O's lone pair of electrons attract forming an aquo complex with a strong Ni-O interaction.³⁸ The resulting shift in electron density of -OH towards O creates a partially positive hydrogen eventually resulting in a hydrolysis reaction seen in equation four followed by an olation condensation reaction in equation five³⁸:



Previous work on a wide variety of commercially available hydrated metal nitrate salts has shown that after thermal decomposition, the varying charge densities of transition metals influence the metal-nitrate bond accordingly.³⁸ Metal ions that have a high charge and small ionic radius polarize the electron cloud of the nitrate lowering the N-O bond order promoting nitrate disassociation, while cations with a lower charge density do not effectively polarize the nitrate electron cloud alluding to the influence different metals impart on the local coordination environment.³⁸ Additional work has also shown that mixed solutions of Al³⁺ and La³⁺ synthesized from nitrate precursors change

the solution pH enough that the oligation condensation product distribution shifts promoting Al^{3+} rich clusters.³⁸

1.5. General Principles of Microwave Chemistry

Microwave-chemistry has been used for the one-pot synthesis of a wide variety of nanostructured materials that can change the kinetics, selectivity and yield of chemical reactions and is based on the ability of a specific material to convert microwave energy and into heat.³⁹ Microwave-assisted chemistry differs from other chemical reactions that proceed by direct absorption of heat, with the two main heating mechanisms of microwave chemistry being dipolar polarization and ionic conduction.³⁹ Dipolar polarization is the result of a solvent constantly trying to align itself within an oscillating electric field (Figure 6a).³⁹ Ionic conduction results in heat generated by ions in solution generating molecular friction with other ions in solution in response to an applied electric field, as seen in Figure 6b.³⁹

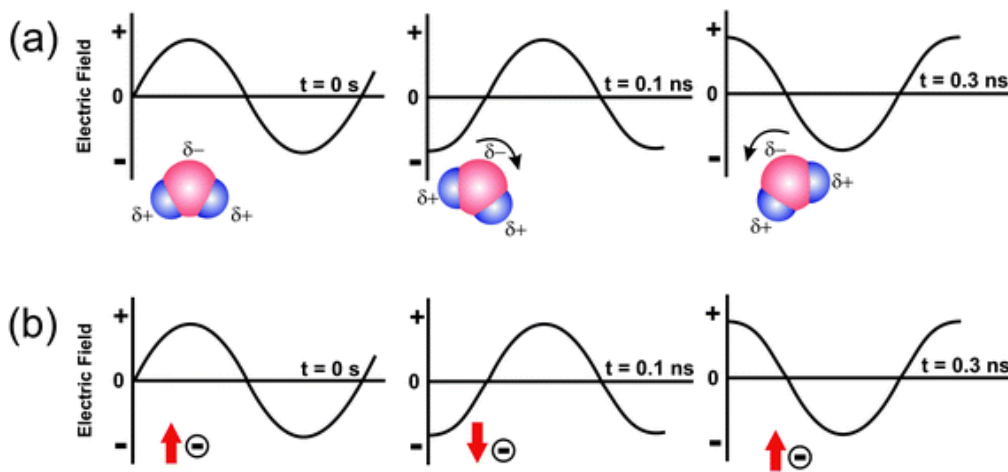


Figure 6. Principles of microwave heating. A) dipolar polarization, B) ionic conduction.³⁹

A solvent's ability to respond to an electric field is an important consideration because different amounts of heat are generated depending on the solvent's specific response to an applied field (i.e. some solvents deliver more heat than others).³⁹ This enables

microwave chemistry to deliver near instantaneous uniform heating throughout the entire reaction vessel since it is independent of thermal conductivity and thermal gradients of the materials in solution unlike conventional heating methods that rely on conductive heating.³⁹ Temperature and heat delivery methods of reaction routes strongly influence nucleation and growth events of nanomaterials.³⁹

Microwave chemistry offers: (i) high heat delivery rates increasing reaction rates without direct contact with the heat source, (ii) near instantaneous heat delivery which conveys a higher level of control, (iii) selective heating (if the solution contains materials with different microwave absorptions the frequency can be tuned to selectively heat a specific species within the solution), (iv) higher yields, (v) reduced side reactions, and (vi) high throughput.³⁹ With reduced reaction times, higher yields, and greater selectivity, microwave chemistry is a greener and more efficient alternative to many other synthetic routes.

Microwave chemistry has been used for the synthesis of many different type of transition metal oxides and hydroxides for use as high powered supercapacitors.⁴⁰ The specific microwave techniques used to synthesis α -Ni(OH)₂^{41,42} or metal-substituted (Ni/Mn/Co⁴³, Ni/Al/Zn⁴⁴, Ni/Co^{45,46}) derivatives of α -Ni(OH)₂ include microwave assisted reflux^{41,45}, microwave assisted hydrothermal techniques^{42,46}, and microwave assisted base catalyzed precipitation.⁴⁴

1.6. Project Motivation and Objectives

The Rhodes group at Texas State University group recently reported on a rapid microwave–assisted hydrothermal synthesis of α -Ni(OH)₂ nanosheets using weakly acidic conditions as a precursor to high-activity oxygen evolution reaction electrocatalysts.⁴⁷

The synthetic route used was adapted from a previously reported method³⁶ to meet the requirement of the group's smaller microwave reactor, resulting in a scaled down synthesis that reduced the reaction volume by a factor of 10 showing the flexibility of microwave chemistry. However, no prior studies have investigated the microwave synthesis of metal substituted α -Ni(OH)₂ nanosheets for use as a cathode in an aqueous rechargeable Ni-Zn battery system.

The objectives of this investigation were to evaluate the effect of substitution of different metal ions (aluminium, cobalt, manganese, zinc) into microwave synthesized α -Ni(OH)₂ and determine their effects on morphology, structure, and electrochemical charge storage. The metal substituted α -Ni(OH)₂ nanosheets were fabricated into device relevant electrodes in order to evaluate their electrochemical performance in coin cells versus monolithic NRL's revolutionary Zn sponge anodes.

The project's key hypothesis were (i) the microwave assisted hydrothermal synthesis of a high surface area, nanostructured substituted α -Ni(OH)₂ nanosheets material can be adapted to incorporate Al³⁺, Co²⁺, Mn²⁺, and Zn²⁺ into the structure by the partial substitution of Ni²⁺ for Al³⁺, Co²⁺, Mn²⁺, and Zn²⁺ at a Ni-M ration of 9:1 and (ii) high capacity Ni(OH)₂ materials may be obtained by using substituents and surface interactions to stabilize the structural changes and distribute electron density necessary for multielectron charge-storage processes within α -Ni(OH)₂.

2. EXPERIMENTAL

2.1. Microwave Synthesis of Ni(OH)₂ Nanosheets

The α -Ni(OH)₂ nanosheets were synthesized using a microwave-assisted hydrothermal method, modified from our previously reported methods^{47, 48} for a large format reactor at the Naval Research Laboratory. All chemicals were obtained from Sigma-Aldrich unless otherwise noted. In an unsubstituted α -Ni(OH)₂ synthesis, Ni(NO₃)₂·6H₂O (3.0 g) and urea (2.46 g) were added to a solution of ethylene glycol (63 mL) and ultrapure water (9 mL, ≥ 18 M Ω -cm used for all subsequent reactions). The solution was exposed (unstirred) to variable microwave radiation (CEM Mars 5 Digestion Microwave System microwave reactor) at 120°C for 39 min. The green precipitate was collected by centrifugation and washed five times with water, three times with ethanol (200 proof, Warner-Graham Company), and then dried overnight at 60°C.

Metal substituted α -Ni(OH)₂ nanosheets (notated as Ni-*M*₁₀; *M*= Al³⁺, Co²⁺, or Zn²⁺) were synthesized by adapting the previously described microwave synthesis with a partial substitution at a Ni²⁺-to-*M*^{z+} ratio of 9:1 (i.e. 10 atomic % substituent for total metal content). In the modified synthesis, either Al(NO₃)₃·9H₂O (0.387 g) Co(NO₃)₂·6H₂O (0.30 g), or Zn(NO₃)₂·6H₂O (0.306 g) were added to a solution of ethylene glycol (63 mL), Ni(NO₃)₂·6H₂O (2.7 g), and urea (2.46 g) in 9 mL of ultrapure water. The solution was then microwaved at 120°C for 39 min. The precipitate was collected and processed as described above with the synthesized and washed materials seen in Figure 7.

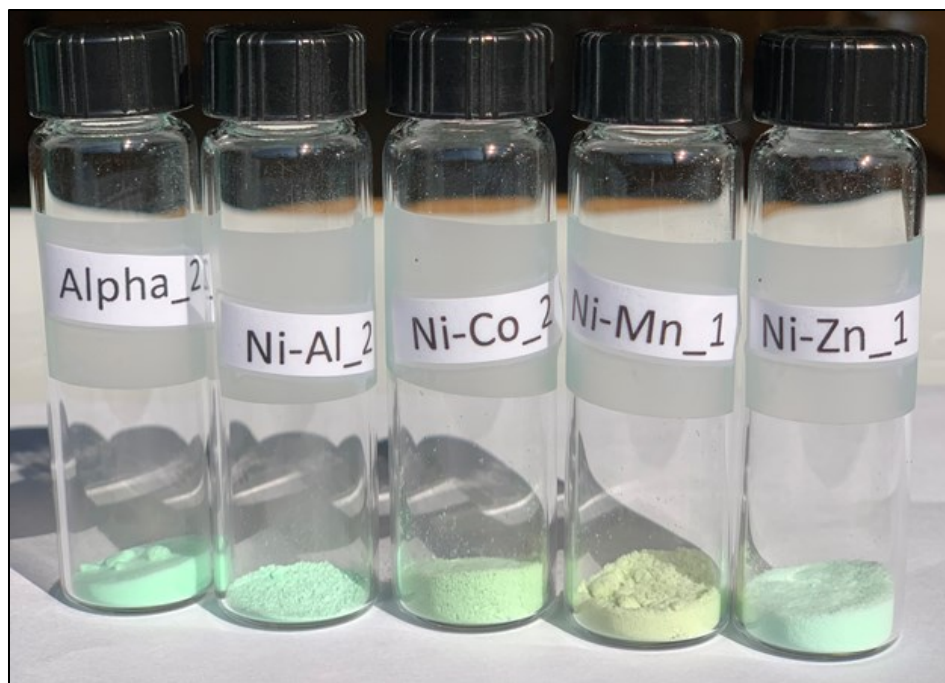


Figure 7. Images of ~25mg of each microwave synthesized nanosheets powder. Unsubstituted α -Ni(OH)₂, Aluminum-substituted α -Ni(OH)₂ (Ni-Al₁₀), Cobalt-substituted α -Ni(OH)₂ (Ni-Co₁₀), Manganese-substituted α -Ni(OH)₂ (Ni-Mn₁₀), and Zinc-substituted α -Ni(OH)₂ (Ni-Zn₁₀).⁴⁹

Select samples were synthesized using a small-scale reactor at Texas State University. In a typical synthesis of α -Ni(OH)₂ nanosheets, Ni(NO₃)₂·6H₂O (1.0 g, Ward's Science) and urea (0.82 g, VWR Analytical) were added to solution of ethylene glycol (21 mL, VWR Analytical) and ultrapure water (3 mL \geq 18 M Ω -cm). The solution was then exposed, to variable microwave radiation (CEM Discover SP Microwave System microwave reactor) while magnetically stirred at 120°C for 13 min. Metal substituted α -Ni(OH)₂ nanosheets (Ni-M₁₀; M= Mn²⁺ or Zn²⁺) were similarly synthesized at Texas State University. For the synthesis of Ni-Mn₁₀ and Ni-Zn₁₀, Mn(NO₃)₂·4H₂O (0.086 g, Alfa Aesar), or Zn(NO₃)₂·6H₂O (0.102 g) were added to a solution of containing ethylene glycol (21 mL, VWR Analytical), ultrapure water (9 mL), Ni(NO₃)₂·6H₂O (0.9 g), and urea (0.82 g, VWR Analytical). The solution was microwaved at 120°C for 13 min. The precipitate was collected and processed as described above.

2.2. Materials Characterization

Morphology was probed using scanning electron microscopy (SEM; FEI-Helios Nanolab 400). Nitrogen physisorption measurements were conducted using a Micromeritics ASAP 2020, where the sample was initially degassed under vacuum at 120°C for 16 h. Specific surface area was determined by Brunauer–Emmett–Teller (BET) analysis while pore diameters and pore volume were determined by Barrett–Joyner–Halenda (BJH) analysis of the desorption isotherm. Elemental analysis of the amount of Ni and *M* within Ni-Al₁₀, Ni-Co₁₀, Ni-Mn₁₀, and Ni-Zn₁₀ was determined from inductively coupled plasma atomic emission spectroscopy (ICP-AES) of digested samples performed by Galbraith Laboratories (Knoxville, Tn.). Powder X-ray diffraction measurements (XRD) were performed using a Bruker AXS D8 Advanced powder X-ray diffractometer with a Cu K_α radiation source, operating at 40 kV and 25 mA and a high-resolution energy-dispersive 1D Linxeye XE detector with a 2θ scan range between 5–80° with a 0.01 increment. Raman spectroscopy experiments were carried out using a Horiba LabRam HR evolution confocal Raman spectrometer equipped with a backscattering geometry and a 600 grooves/mm grating. A 514 nm argon-ion laser line operating at 300 mW power, measured at the laser head, was focused through a 50×-objective Olympus microscope with a neutral density filter of 50%, and the instrument was calibrated using the 520.7 cm⁻¹ band of Si. The sample was inspected using the optical microscope before/after exposure to the laser to ensure sample was not visually damaged.

2.3. Electrochemical Characterization

2.3.1. *Electrode Fabrication*

Ni-foam current collectors (MTI Corp.) were punched out (round, ½ inch diameter) and cleaned as recommended by the manufacturer which consisted of sonicating in an ice bath for 5 min each in concentrated hydrochloric acid (Fisher Scientific), water, and ethanol (200 proof, Warner-Graham Company). The current collectors were then dried for 10 minutes under vacuum at 60 °C to remove residual ethanol. Composite cathodes were fabricated by preparing a slurry composed of the active material (α -Ni(OH)₂, Ni-Al₁₀, Ni-Co₁₀, Ni-Mn₁₀, or Ni-Zn₁₀), carbon (100% compressed, 99.9%+ acetylene black, Alfa Aesar) and binder (PTFE dispersion in water, Sigma Aldrich, 665800) using a weight percent ratio of 70:25:5 for the active material, conductive carbon, and binder, respectively. For preparing the slurry, the active material (~60 mg) and conductive carbon (~21.4 mg) were mixed by hand with an agate mortar and pestle and then combined with 12–15 drops of water in a vial. The slurry was then treated in a bath sonicator for 10 minutes after which the binder was added, and then the slurry was sonicated for a further 10 minutes. The Ni foam current collectors were then immersed in the slurry and treated under vacuum for 30 min. The cathodes were dried under ambient conditions overnight, and then further dried at 60 °C for 2 h before pressing the composite through a pasta roller (Imperia).

Nickel-zinc coin cells were constructed in a similar manner to that previously reported by researchers at the Naval Research Laboratory using a “Gen III” zinc sponge as the anode inside a gas-tight laser-cut acrylic alkaline-resistant coin cell (Figure 8) as previously reported.¹⁴

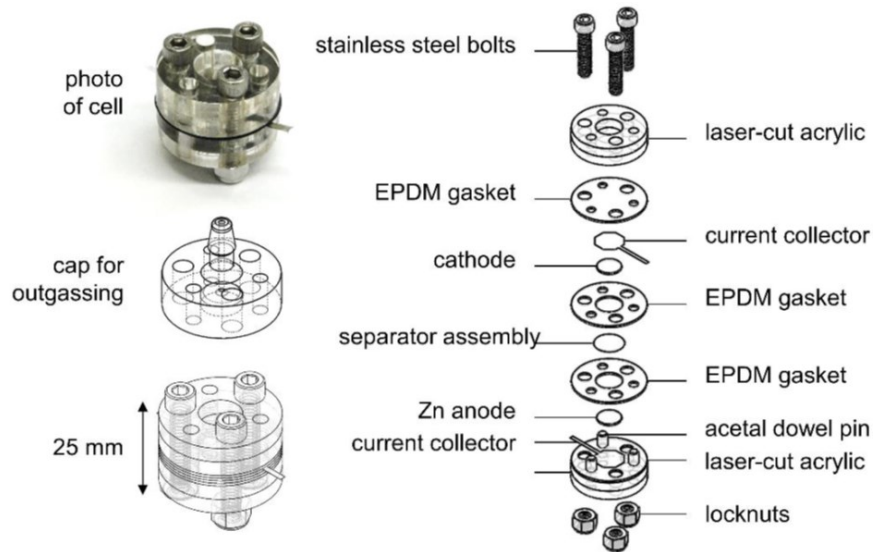


Figure 8. Schematic representation of laser cut-gas tight- acrylic battery cells.¹⁴

Briefly, the cells were constructed (from the anode up) with a tin foil current collector (0.25 mm thick, 99.8% Alfa Aesar), Gen-III Zn-sponge anode Celgard separator (3501), Freudenberg separator (700/28), carbon composite cathode embedded in Ni foam, expanded Ni-mesh current collector (Dexmet), and a second Freudenberg separator within gas-tight ethylene propylene diene monomer (EPDM) gaskets. Before cell assembly, the cathode, Celgard, and Freudenberg separators were vacuum infiltrated with a 6 M KOH/1 M LiOH electrolyte for 30 min, while the zinc sponge was vacuum infiltrated for the same amount of time in a dispersion of 11 wt% Ca(OH)₂ in 6 M KOH/1 M LiOH.⁵⁰ The coin-cell experiments were designed such that the capacity of the active cathode material in the cell was significantly lower than the Zn anode capacity enabling a study of the cathode material within a cathode-limited cell configuration.

2.3.2. Electrochemical Characterization

Galvanostatic experiments were carried out using an Arbin battery cycler. The cells were charged and discharged at a mass-normalized current rate of 84.4 mA g⁻¹ (0.2 C based on a theoretical capacity of 422 mAh g⁻¹_{active} for α-Ni(OH)₂) between 1.3 and

2.0 V. During charging and discharging, if the cells theoretical capacity (422 mAh g^{-1} i_{active}) was reached before the upper voltage limit, the cell automatically began discharging. The mass of active material (α -Ni(OH)₂, Ni-Al₁₀, Ni-Co₁₀, Ni-Mn₁₀, or Ni-Zn₁₀) was calculated to be 70% of the weight of the electrode after subtracting the mass of the Ni foam. These cycling conditions were chosen specifically to study the effect that the metal substituents impart on the redox and OER voltages of α -Ni(OH)₂ and are not optimized charging conditions for battery performance.

Variations between electrodes were evaluated and normalized using statistical analysis. Using four distinct samples (Commercially available β -Ni(OH)₂, Alfa Aesar: 12054-48-7, or microwave-synthesized Ni-Co, Ni-Al and α -Ni(OH)₂) several different electrodes were fabricated and galvanostatic experiments were carried out. The standard deviation of the samples discharge capacity were averaged across 3 different cycles (1st, 15th, and 30th).

Differential capacity analysis (dQ/dV) was performed in Origin by taking the derivative of the mass-normalized capacity with respect to the cell's voltage. The resulting dQ/dV plots were smoothed within Origin (FFT Filter) removing all the high frequency signals. The subsequent mass-normalized dQ/dV plots were fit with Origin's Fit Peak Pro which uses a Levenberg-Marquardt (L-M) algorithm.

As a result of the corona virus pandemic (COVID-19) that required Texas State University to impose social distancing and impose lab restrictions some samples were not be repeated prior to completing this thesis. At this time and in this present work, Ni-Mn₁₀ and Ni-Zn₁₀ data should be considered preliminary results.

3. RESULTS AND DISCUSSION

3.1. Analysis of Morphology and Porosity

The impacts on the nanosheet morphology characteristic of microwave-synthesized α -Ni(OH)₂ upon substituting Al³⁺, Co²⁺, Mn²⁺, or Zn²⁺ for Ni²⁺ at a 9 Ni:1 M atomic ratio were studied by scanning electron microscopy (SEM). The SEM images of unsubstituted α -Ni(OH)₂ (Figure 9a) shows large round aggregates (diameters of $\sim 1.5 \mu\text{m}$) of individually interconnected nanosheets.

The overall nanosheet morphology was maintained at a synthetic metal substitution of 10 at% (Figure 9b-e). Compared with unsubstituted α -Ni(OH)₂, substitution with Al³⁺ effected sheet growth by producing smaller more-dense interwoven nanosheets with Ni-Al₁₀ (Figure 9b), which in turn affected the overall nanosheet aggregate growth by producing smaller (diameters of $\sim 0.5 \mu\text{m}$) more visually dense round aggregates of interconnected nanosheets. Ni-Co₁₀ (Figure 9c) had larger aggregates (diameters of $\sim 4 \mu\text{m}$) of nanosheets when compared with unsubstituted α -Ni(OH)₂. Similarly, Ni-Mn₁₀ (Figure 9d) had larger nanosheet aggregates (diameters of $\sim 3 \mu\text{m}$). Ni-Zn₁₀ (Figure 9e) had the largest nanosheet aggregates (diameters of $\sim 10 \mu\text{m}$) while retaining a surface morphology most similar to unsubstituted α -Ni(OH)₂.

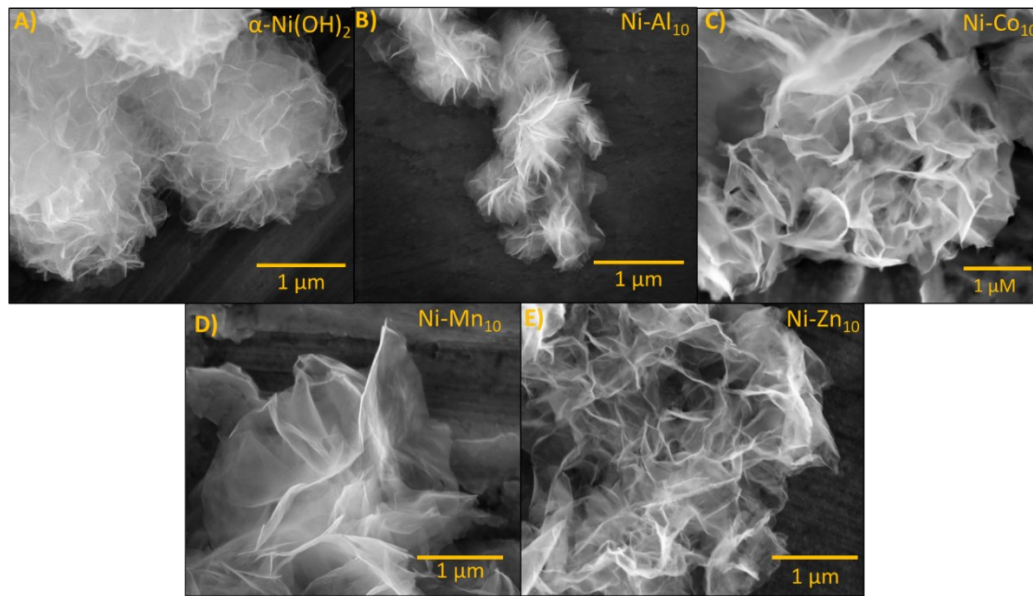


Figure 9. Scanning electron micrographs of microwave synthesized nanosheets. a) Unsubstituted α -Ni(OH)₂ nanosheets, b) Aluminum-substituted nanosheets (Ni-Al₁₀), c) Cobalt-substituted nanosheets (Ni-Co₁₀), d) Manganese-substituted nanosheets (Ni-Mn₁₀), and e) Zinc-substituted nanosheets (Ni-Zn₁₀).⁴⁹

The changes observed in the morphologies of the microwave synthesized nanosheets may be influenced by a number of phenomena including, the charge densities (CD) of the metal ions relative to Ni²⁺ and the solubility product constants (K_{sp}) of the metal hydroxides. Ni-Al₁₀ with a higher charge density (C.D. of Al³⁺ = 4.68 z nm⁻³³⁸, where z is the atomic number) produced smaller more dense nanosheet aggregates while the substituents with a lower charge density relative to nickel (Co²⁺; 1.15 z nm⁻³, Mn²⁺; 0.84 z nm⁻³, and Zn²⁺; 1.18 z nm⁻³)³⁸ produced larger nanosheet aggregates.³⁸ Other studies have related the difference in morphology to the solubility of the metal-hydroxide products (K_{sp} of Al(OH)₃ = 1.3 x 10⁻³³, < Co(OH)₂ = 5.9 x 10⁻¹⁶ < Ni(OH)₂ = 5.5 x 10⁻¹⁶ < and Mn(OH)₂ (1.9 x 10⁻¹³), and speculate that because the K_{sp} of Al(OH)₃ is much smaller compared to Ni(OH)₂ Al³⁺ might deposit into the Ni(OH)₂ lattice more rapidly than Ni²⁺, Co²⁺, or Mn²⁺ leading to irregularities in morphology compared to pure α -Ni(OH)₂ samples.^{24, 51} The higher charge density of Al³⁺ combined with the smaller K_{sp}

of Al(OH)₃ could affect the nucleation and aggregation of the nanosheets by constraining the crystallite growth. The possible role of different charge densities of the metal ions on the aqueous coordination environment and the resulting effect on hydrolysis and condensation reactions leading to growth of Ni(OH)₂ nanosheets is further discussed below.

Nitrogen physisorption was used to determine the influence of substituents on the electrochemical BET surface area, average-pore diameters, and cumulative desorption pore volume (Table 1). The BET surface area of unsubstituted α -Ni(OH)₂ was 95 m² g⁻¹ with an average BJH desorption pore diameter of 14.1 nm, and a larger BJH desorption cumulative pore volume of 0.668 cm³ g⁻¹ than previously reported for microwave synthesis of α -Ni(OH)₂ but comparable to the Rhodes groups' previously reported method using a scaled down synthesis with a smaller microwave reactor.^{41, 47}

Table 1. Nitrogen Porosimetry of metal substituted nanosheets.⁴⁹

Sample	BET surface area (m ² g ⁻¹)	Pore diameter (nm)	Pore volume (cm ³ g ⁻¹)
α -Ni(OH) ₂	95	14.1	0.668
Ni-Al ₁₀	40	16.2	0.426
Ni-Co ₁₀	57	18.5	0.302
Ni-Mn ₁₀	74	22.0	0.382
Ni-Zn ₁₀	100	17.5	0.514

Substituents with a smaller atomic number relative to Ni²⁺ (Al³⁺, Co²⁺, and Mn²⁺) decreased the overall surface area while substituents with a larger atomic number (Zn²⁺) increased the BET surface area. With a surface area of 40 m² g⁻¹, Al³⁺ had the greatest impact on BET surface area confirming what was observed in the SEM micrographs: that the Ni-Al₁₀ material had more dense aggregates of interconnected nanosheets. Ni-Co₁₀ (57

$\text{m}^2 \text{g}^{-1}$) and Ni-Mn_{10} ($74 \text{ m}^2 \text{g}^{-1}$) had lower overall surface area compared with unsubstituted $\alpha\text{-Ni(OH)}_2$, but not to the same extent as Ni-Al_{10} . Zn^{2+} was the only substituent studied that increased the BET surface area ($100 \text{ m}^2 \text{g}^{-1}$ for Ni-Zn_{10}). All substituents increased the pore diameter of the microwave synthesized nanosheets while the pore volume decreased. As discussed above, changing the initial synthetic solution from a nickel nitrate solution to a mixed nitrate solution can affect the olation products and impact the morphology and porosity.³⁸

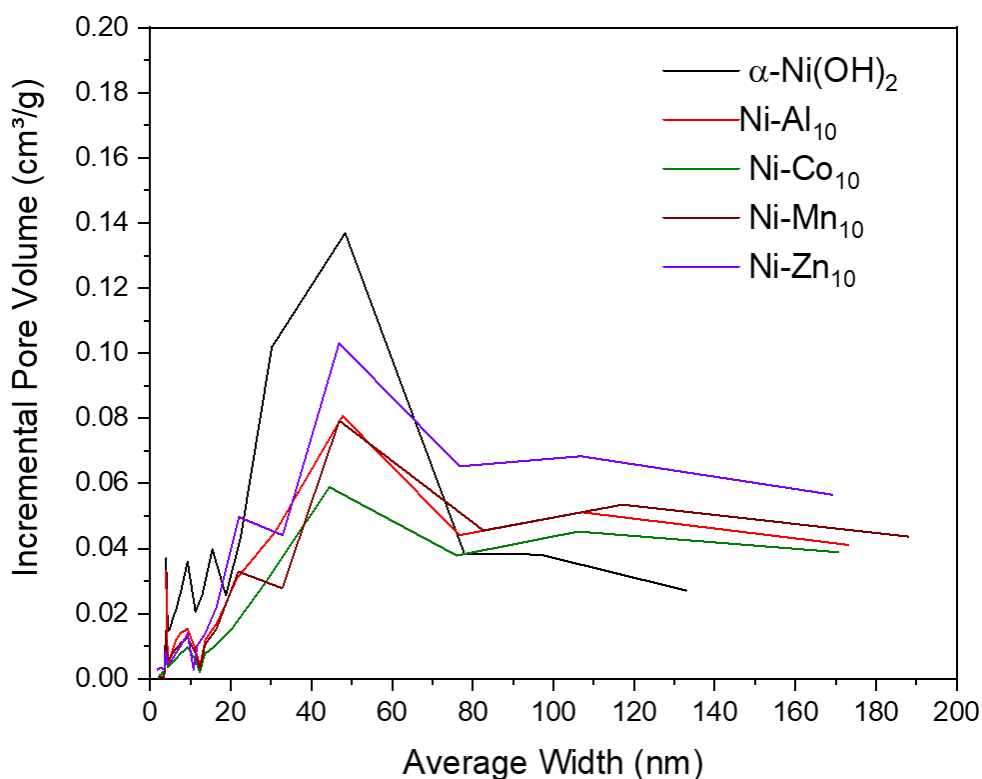


Figure 10. Barrett–Joyner–Halenda desorption pore distribution plots. Comparison of unsubstituted and substituted nanosheets.⁴⁹

The pore size distribution plot (Figure 10) indicated that the majority of pores for all samples were in the mesopore ($>2\text{nm}-50\text{nm}$) and macropore range ($>50 \text{ nm}$), an advantageous trait in electrochemical applications which improves the access to the electrolyte solution at diffusion rates approaching open solution.^{47, 52} The pore volume in

the mesopore range appears to decrease with substitution, with Co²⁺ substitution having the lowest mesopore volume.

3.2. Analysis of Composition

During the synthesis, all metals were substituted into the reaction at a Ni:M ratio of 9:1 (nominal molar ratios of Ni_{0.9}M_{0.1}). Elemental analysis of the Ni:M content was determined for Ni-Al₁₀, Ni-Co₁₀, Ni-Mn₁₀, and Ni-Zn₁₀ (Table 2).

Table 2. Elemental analysis of unsubstituted and metal-substituted nanosheets detected by inductively coupled plasma optical emission spectral (ICP-OES) analysis of Ni:M ratio of metal substituted nanosheets.⁴⁹

Sample name	Relative atomic % from synthesis	Relative atomic % from ICP analysis
α -Ni(OH) ₂	–	–
Ni-Al ₁₀	Ni _{0.90} Al _{0.10}	Ni _{0.86} Al _{0.14}
Ni-Co ₁₀	Ni _{0.90} Co _{0.10}	Ni _{0.90} Co _{0.10}
Ni-Mn ₁₀	Ni _{0.90} Mn _{0.10}	Ni _{0.97} Mn _{0.03}
Ni-Zn ₁₀	Ni _{0.90} Zn _{0.10}	Ni _{0.81} Zn _{0.19}

Ni-Al₁₀ and Ni-Zn₁₀ were both found to have a higher experimental Ni:M ratio than the initial synthetic ratios with a relative composition of Ni_{0.86}Al_{0.14} and Ni_{0.81}Zn_{0.19}. The Ni:Co ratio of Ni-Co₁₀ matched the initial synthetic ratio with a relative composition of Ni_{0.90}Co_{0.10}. While Ni-Mn₁₀ was found to have a lower experimental Ni:M ratio than the initial synthetic ratios with a relative composition of Ni_{0.97}Mn_{0.03}.

As discussed in Section 1.4, the charge densities of transition metals have been shown to influence the metal-nitrate bond during thermal decomposition. In aqueous solutions, the charge densities also influence the lability of M-H₂O (equation 4).³⁸ The ionic radius and differing ligand field strengths of metal cation influence the reaction rate.³⁸ Metal ions with larger ionic radius typically have a higher lation rate while cations with higher

ligand field strength have a lower rates of olation due to a greater orbital overlap between metallic d-orbitals and H₂O.³⁸ The differing rates of the hydrolysis and condensation reactions, the variation in ionic radii, and differences in the initial solvation spheres between Ni²⁺ and the substituents may account for some of but not all of the differences between the Ni:M atomic % between determined from ICP and initial synthetic substitution ratios. Studies on thin films mixed-metal oxides synthesized from mixed-metal nitrates solutions found that the changes in pH can result in changes in morphology, porosity, and metal concentration, preferentially driving the reaction of one metal over another.³⁸As discussed above, the solubility rate constant (K_{sp}) of the reaction products may also influence the rate at which some metals are incorporated into the α -Ni(OH)₂ structure compared to others. The aforementioned phenomena may all be occurring simultaneous and while interacting with other molecules in the reaction media (ethylene glycol, urea, and nitrate) may further factor into the substituents identity influencing the amount incorporated into α -Ni(OH)₂.

3.3 X-ray Diffraction Characterization

The effects of Al³⁺, Co²⁺, Mn²⁺, or Zn²⁺ substituents on the crystal structure of α -Ni(OH)₂ nanosheets were studied by powder X-ray diffraction (Figure 11). Unsubstituted α -Ni(OH)₂ nanosheets exhibit three prominent diffraction peaks: a sharp low angle peak at 2θ of 11.28°, medium relative intensity peak at 2θ of 33.32°, and a medium relative intensity high angle peak at 2θ of 59.56° which are consistent with the alpha phase of Ni(OH)₂ and are assigned as the (001), (110), and (300) planes respectively.¹⁵

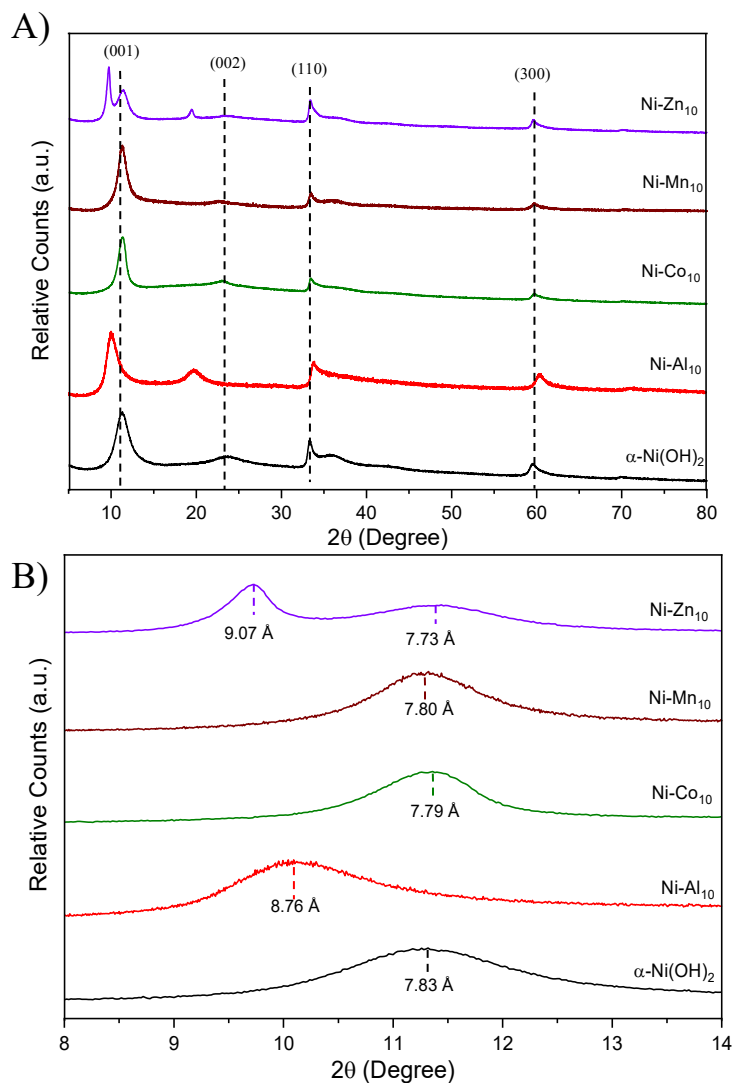


Figure 11. X-ray diffraction spectra of microwave synthesized nanosheets. A) 2θ scan range between 5–80°. B) Expanded region for a 2θ scan range between 9–14° showing changes in X-ray diffraction spectra of the (001) plane associated with the interlayer spacing of α -Ni(OH)₂⁴⁹

The (001) plane represents the interlayer spacing between Ni(OH)₂ layers containing loosely bound water or other anions and provides information on the degree of hydration with shifts in this peak corresponding to a larger or smaller interlayer spacing.^{15, 26, 27} The effects of substitution on the (001) plane of α -Ni(OH)₂ are presented in Table 3. A broad peak at a 2θ of 23.72, is assigned as (002)- a reflection which is related to the (001) plane. The asymmetric (110) plane represents the turbostratic disorder characteristic of α -

Ni(OH)₂.^{17, 26, 53}

Table 3. Interlayer crystallographic peak position and interlayer spacing of microwave synthesized nanosheets determined from X-ray diffraction.⁴⁹

Sample	(001) Peak position (2 θ)	d-spacing (Å)
α -Ni(OH) ₂	11.28	7.83
Ni-Al ₁₀	10.08	8.76
Ni-Co ₁₀	11.34	7.79
Ni-Mn ₁₀	11.33	7.80
Ni-Zn ₁₀	11.42	7.73

Ni-Al₁₀ shifted the (001) peak from a 2 θ of 11.28° to 10.08° resulting in an increase in the interlayer spacing from 7.83 Å to 8.76 Å which has been attributed to an influx of negatively charged anions such as NO₃⁻, OH⁻, or CO₃⁻ required to balance an increased electrostatic charge between the Ni(OH)₂ layers resulting from the partial substitution of a divalent cation (Ni²⁺) for a trivalent cation (Al³⁺).^{23, 26, 27} The diffraction pattern of Ni-Zn₁₀ showed a new low angle peak at a 2 θ of 9.72° which has not been observed in previous studies of Zn²⁺ substituted α -Ni(OH)₂.^{35, 36, 54} The new low angle peak of Ni-Zn₁₀ could be a result of Zn²⁺ not completely incorporating into the lattice structure of Ni(OH)₂⁵¹ and could indicate to a mixed phased material. A previous study of a layered vanadium oxide material⁵⁵ showed that the vanadium oxide layers were pillared by interlayer water and Zn²⁺ ions, and it seems plausible that the new low angle peak at a 2 θ of 9.72° observed with Ni-Zn₁₀ may be a Zn rich peak corresponding to an interlayer region pillared by Zn²⁺ while the peak at a 2 θ of 11.42° is not pillared by Zn²⁺.

3.4. Raman Spectroscopic Characterization

Raman spectroscopy was utilized to probe the effect substitution plays on the local coordination environment of the Ni(OH)₂ symmetric (A_{1g}) and asymmetric (E_g) lattice

modes,^{56, 57} hydroxyl modes,⁵⁷ and evaluate the presence of additional compounds that may have been incorporated in the structure from the initial synthesis¹⁵ such as nitrates,⁵⁷ ethylene glycol,⁵⁸ or urea.⁵⁹ An operando Raman spectroscopy study correlated shifts in the $\nu(E_g)$ and $\nu(A_{1g})$ frequencies with charge storage.⁵⁶ “Blue shifts” or shifts to larger wavenumbers of both E_g and A_{1g} lattice modes corresponded to charge being stored and resulted in a change in electron cloud distribution and a subsequent shortening of the Ni-O bond while “red shifts” or shifts to smaller wavenumbers corresponded to a longer Ni-O bond and a release of stored charge.⁵⁶ The presence of nitrate modes within the Raman spectra may indicate nickel-nitrate coordination.^{38, 57} First row transition metal (Ni, Co, and Zn)-nitrate complexes form from the hydrated metal complex due to their low thermodynamic stability (low free energy of hydration) resulting from weak ligand field effects that weaken the M-H₂O bond in solution allowing for the formation of a metal-nitrate complex represented by the following equation.³⁸



Based on equation 6, it seems likely that nitration occurs before the microwave-assisted hydrolysis and condensation reactions begins. From a prior study, the inclusion of nitrates into the interlayer region of α -Ni(OH)₂ is not detrimental to the electrochemical performance of the material, and nitrates are preferable to sulfates.²⁶

The Raman peaks of microwave synthesized unsubstituted α -Ni(OH)₂ (Figure 12) between 50-4000 cm⁻¹ have been labeled and are summarized in Table 4. The Raman peaks below 250 cm⁻¹ are associated with long range torsional modes. The peak at 458 cm⁻¹ was assigned as the doubly degenerate $\nu(E_g)$ lattice mode of α -Ni(OH)₂, however, the singly degenerate $\nu(A_{1g})$ lattice mode-expected at 495-554 cm⁻¹ is absent.⁵⁶

⁵⁷ The intensity of the $\nu(A_{1g})$ mode has been reported to change with polarization.⁵⁶

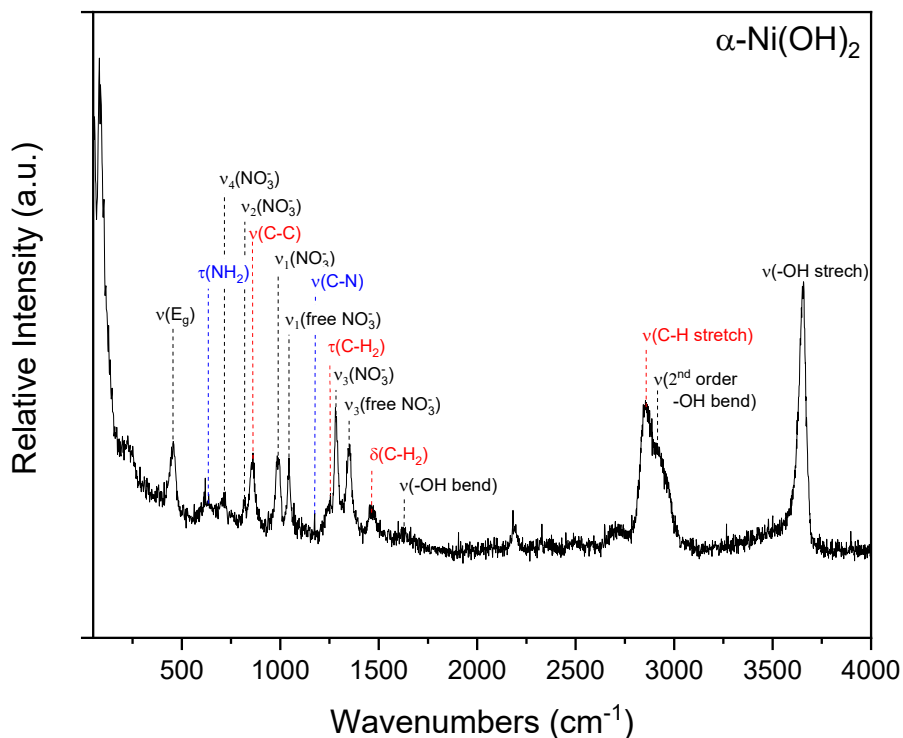


Figure 12. Raman spectra of unsubstituted α -Ni(OH)₂ with peak assignments. Raman spectra of unsubstituted microwave synthesized α -Ni(OH)₂ nanosheet within the 50 cm⁻¹ to 4000 cm⁻¹ region; spectra obtained using an excitation laser frequency of 514 nm.⁴⁹ The peak assignments of the local coordination environment of the Ni(OH)₂ lattice modes,⁵⁶ hydroxyl modes,⁵⁷ and additional compounds that have been incorporated in the structure from the initial synthesis are labeled.^{15, 56-59}

The Raman spectra showed multiple peaks between 700 cm⁻¹ and 1600 cm⁻¹. A previous Raman and infrared study on Ni(OH)₂ electrodeposited onto thin films assigned multiple nitrate modes with α -Ni(OH)₂ and identified two distinct nitrate chemical environments with some nitrate located in the interlayer.⁵⁷ The frequency of the four nitrate modes and two “free” nitrate modes of the microwave-synthesized α -Ni(OH)₂ nanosheets are in general agreement with previous results (compared in Table 4). The changes in frequency might be due to interactions between the α -Ni(OH)₂ lattice, nitrates and the precursor chemicals ethylene glycol and urea that were not used in other synthesis routes.

Table 4. Experimental and reported literature values of Raman peak assignments of unsubstituted microwave-synthesized α -Ni(OH)₂ nanosheet within the 50 cm⁻¹ to 4000 cm⁻¹ region.⁴⁹

Signal Source	Peak Assignment	Experimental wavenumber (cm ⁻¹)	Literature wavenumber (cm ⁻¹)
α -Ni(OH) ₂ lattice	$\nu(E_g)$	458	460 ⁵⁷ 474 ⁵⁶
	$\nu(A_{1g})$	–	495 ⁵⁷ 554 ⁵⁶
	$\nu(-OH \text{ bend})$	1625	1620 ⁵⁷
	$\nu(2^{ND} \text{ order } -OH \text{ bend})$	2914	~ 2900 ⁵⁷
	$\nu(-OH \text{ stretch})$	3657	3647 ⁵⁷
Nickel-nitrate precursor	$\nu_1(NO_3^-)$	986	997 ⁵⁷
	$\nu_2(NO_3^-)$	821	816 ⁵⁷
	$\nu_3(NO_3^-)$	1283	1291 ⁵⁷
	$\nu_4(NO_3^-)$	721	719 ⁵⁷
	$\nu_1(\text{free } NO_3^-)$	1042	1047 ⁵⁷
	$\nu_3(\text{free } NO_3^-)$	1352	1350 ⁵⁷
Ethylene glycol precursor	$\nu(C-C)$	861	864 ⁵⁸
	$\tau(C-H_2)$	1254	1260 ⁵⁸
	$\delta(C-H_2)$	1464	1459 ⁵⁸
	$\nu(C-H)$	2854	2875 ⁵⁸
Urea precursor	$\nu(C-N)$	1173	1177 ⁵⁹
	$\tau(NH_2)$	636	642 ⁵⁹

The presence of ethylene glycol coordination originating from the synthetic conditions has been previously reported in cobalt/nickel layered double hydroxides and characterized by FTIR analysis⁶⁰ and may be also coordinating in the microwave-synthesized materials reported here. The Raman vibrational spectra of liquid ethylene glycol includes many peaks between 500 cm⁻¹ and 4000 cm⁻¹.⁵⁸ The microwave

synthesized α -Ni(OH)₂ nanosheets showed four peaks at similar frequencies to those of ethylene glycol (compared in Table 4) with a ν (C-C) at 861 cm⁻¹, τ (C-H₂) at 1254 cm⁻¹, δ (C-H₂) at 1464 cm⁻¹ and ν (C-H) at 2854 cm⁻¹. The ν (C-H) peak at 2854 cm⁻¹ is partially convolved with a second peak at 2914 cm⁻¹ (Figure 12) and attributed to a broad ν (-OH) bending mode. Urea was also present during the synthesis, and two peaks in the Raman spectra of microwave synthesized α -Ni(OH)₂ nanosheets align with a previous work on the vibrational spectra of urea (compared in Table 4).⁵⁹ The sharp peak at 3657 cm⁻¹ is another characteristic peak of α -Ni(OH)₂ corresponding to a lattice ν (-OH) stretching mode and confirming the α -Ni(OH)₂ (the lattice hydroxyl mode of β -Ni(OH)₂ occurs at 3581 cm⁻¹)⁵⁷ phase assignment seen by the x-ray diffraction pattern.⁵⁷

The Raman spectra of Ni-Al₁₀, Ni-Co₁₀ and Ni-Zn₁₀ (Figure 13a) show differences in the relativity intensities of several peaks compared with the other samples. Changes in intensity may be affected by substituents altering quantity of incorporated anions, changes in the electronic environment, electronic states interacting with the laser excitation frequency ($\lambda_{\text{excitation}} = 514 \text{ nm}$), changes in Raman cross section or sample surface area may influence Raman intensity by changing the collection efficiency from the sample.

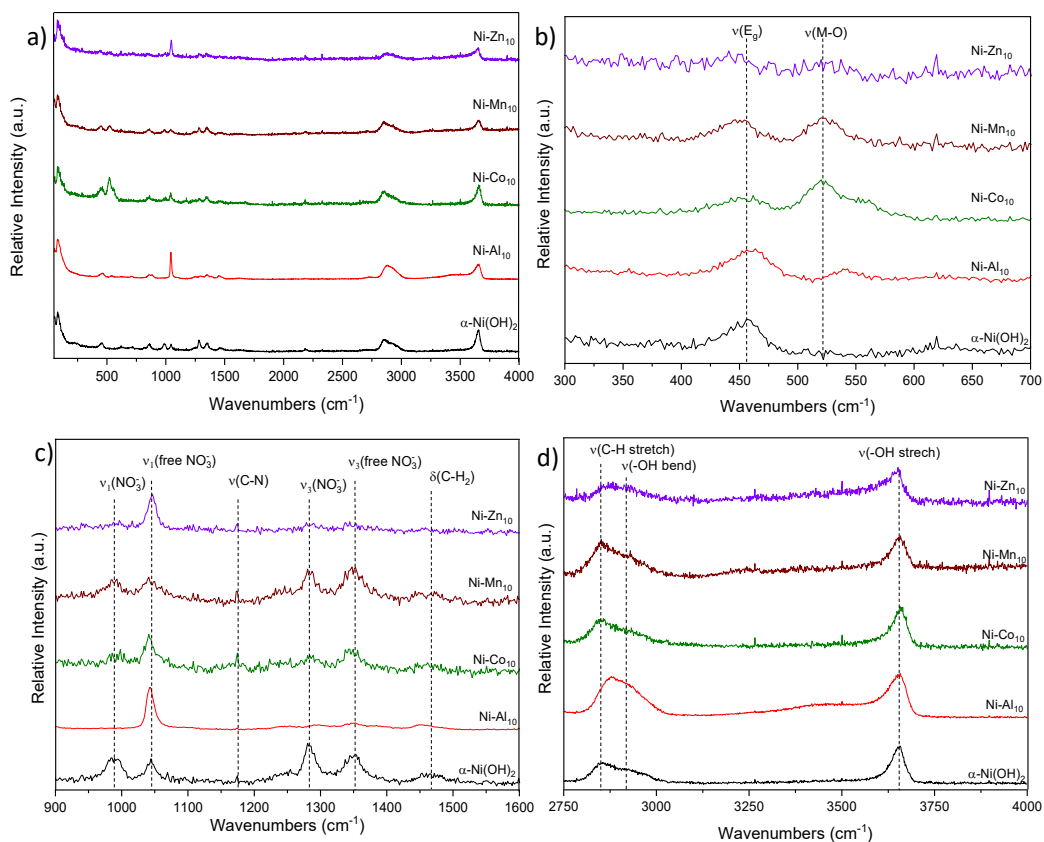


Figure 13. Raman spectrum of substituted α -Ni(OH)₂. The influence of metal substitution on the Raman spectrum of α -Ni(OH)₂ nanosheets within 50 cm⁻¹ to 4000 cm⁻¹; B) the peak assignments of the local coordination environment of the Ni(OH)₂ lattice modes between 300 cm⁻¹ to 700 cm⁻¹; C) the peak assignments of additional compounds incorporated into the structure between 900 cm⁻¹ to 1600 cm⁻¹ region and D) the peak assignments of additional compounds and α -Ni(OH)₂ hydroxyl modes between the 2750 cm⁻¹ to 4000 cm⁻¹ region obtained using an excitation laser frequency of 514 nm.⁴⁹

The $\nu_1(\text{free NO}_3^-)$ peak of Ni-Al₁₀ (Figure 13a) shows a higher relative intensity compared to other samples. The high charge density and high thermodynamic stability (highly negative free energy of hydration) of the Al-OH₂ bond have been associated with much lower rates of nitration (equation 6) compared to the other substituents surveyed.³⁸ It may then be possible that free nitrates are brought into the structure to balance the change in electrostatic charge resulting from the substitution of a divalent cation for a trivalent cation. As discussed above, the nitrate modes of α -Ni(OH)₂ thin films indicated some nitrate anions are located in the interlayer.⁵⁷ Based on the increase in the interlayer

spacing of Ni-Al₁₀ seen by XRD (Figure 11) these charge balancing nitrates may be located in the interlayer region.

Resonance effects may also influence the relative intensities of Raman modes. A prior study supported resonance enhancement effects by observing an increase in signal intensity of the $\nu(E_g)$ and the $\nu(A_{1g})$ of α -Ni(OH)₂ thin films when a Raman laser line with an excitation laser frequency near the UV-Vis absorbance maxima of α -Ni(OH)₂.⁵⁶ The $\nu(E_g)$ and the $\nu(A_{1g})$ lattice modes of Ni-Co₁₀ (Figure 13a) are much more pronounced compared with other samples and may be related to resonance enhancement effects and changes of samples color were observed (Figure 7). Further work is needed to understand the specific effects of the substituents on the electronic structure and their possible influence on the Raman modes. In the case of Ni-Zn₁₀ increases in BET surface area may account for a decrease in intensity of the lattice modes.

The influence of metal substitution on the α -Ni(OH)₂ lattice modes can be observed in Figure 13b. In all metal substituted samples, a new Raman peak arises between 520 cm⁻¹ and 540 cm⁻¹ and may be related to a vibrational mode arising from a metal-oxygen bond of the substituent metal ion. Ni-Al₁₀ shifted the frequency of the $\nu(E_g)$ lattice mode from 458 cm⁻¹ to 463 cm⁻¹ while the new Raman peak observed at 539 cm⁻¹ may be an $\nu(\text{Al}(\text{O}/\text{OH})_n)$ mode which has been previously reported at 530 cm⁻¹.⁶¹ The $\nu(E_g)$ lattice mode frequency shift indicates the local potential energy environment is altered when Al³⁺ is substituted into the α -Ni(OH)₂ structure which is further supported by changes in voltages of the Ni-centered redox peaks (discussed below). With Ni-Co₁₀, the frequency of the $\nu(E_g)$ mode remains unchanged relative to the frequency observed within unsubstituted α -Ni(OH)₂. Two new Raman peaks of Ni-Co₁₀ were observed with Co²⁺

substitution the first peak at 520 cm^{-1} , a frequency lower than that of the new peak found with Ni-Al₁₀ (539 cm^{-1}) and a second peak at 552 cm^{-1} . A previous study on the Raman spectra of Co(OH)₂ observed similar features as observed within the new Raman peaks observed in Ni-Co₁₀ and assigned them as the $\nu(\text{A}_{2\text{u}})$ and $\nu(\text{E}_{\text{g}})$ of Co(OH)₂.⁶² Even though the relative concentration of Mn²⁺ was present at significantly lower concentrations compared to other substituents (discussed in 3.2) it was enough to change the local chemical environment by shifting the $\nu(\text{E}_{\text{g}})$ lattice mode frequency down to 446 cm^{-1} and resulted in new peak at 520 cm^{-1} . Mn-O lattice vibrations have been reported at 523 cm^{-1} in manganosite.⁶³ Within Ni-Zn₁₀ the $\nu(\text{E}_{\text{g}})$ mode showed a lower relative intensity compared to unsubstituted α -Ni(OH)₂ which may be due to the significantly higher surface area of Ni-Zn₁₀ which affects the collection efficiency, the $\nu(\text{E}_{\text{g}})$ mode appears at 440 cm^{-1} , a lower frequency than observed within unsubstituted α -Ni(OH)₂. The new Raman peak associated with Ni-Zn₁₀ occurs at 523 cm^{-1} a similar frequency as the other divalent substituted metals (Ni-Co₁₀ and Ni-Mn₁₀) with prior studies assigning ZnO modes between 480 cm^{-1} and 590 cm^{-1} .^{64, 65}

The additional Raman peaks observed within the metal-substituted samples between 300 cm^{-1} and 700 cm^{-1} and the lack of additional XRD peaks that would indicate the substituted metal ions were within a separate phase supports that the metal substituents are at least partially located within the Ni(OH)₂ lattice. Substitution of Al³⁺ shifted the $\nu(\text{E}_{\text{g}})$ mode to a higher frequencies than that of the other divalent-substituents, which suggests that Al³⁺ interaction within the structure results in shortening of the Ni-O bond, as supported by prior work.⁵⁶ The influence of metal substitution on select Raman peaks are summarized in Table 5.

Nitrate modes are observed in all samples (Figure 13c) at 989 and 1280 cm^{-1} and free nitrates are observed at 1044 and 1350 cm^{-1} , which may originate from the synthetic precursor. The free nitrates may be located in the interlayer region while others are coordinated to metal centers as discussed above.^{57, 60} Ni-Al₁₀ and Ni-Zn₁₀ show a shift to a higher frequency of both the $\nu(\text{C-H})$ stretching and $\nu(-\text{OH})$ bending modes (Figure 13d) associated with ethylene glycol compared to other substituents further indicating that substituents may interact with synthetic precursors changing the local environment of both the $\nu(\text{C-H})$ stretching and $\nu(-\text{OH})$ bending modes when Al³⁺ or Zn²⁺ are substituted into the $\alpha\text{-Ni}(\text{OH})_2$ structure. The frequencies of the $\nu(-\text{OH})$ stretching mode are consistent with $\alpha\text{-Ni}(\text{OH})_2$ phase rather than the $\beta\text{-Ni}(\text{OH})_2$ phase⁵⁷ which are consistent with XRD analysis that supported the structure of the nanosheets being $\alpha\text{-Ni}(\text{OH})_2$. The $\nu(\text{C-N})$ mode of urea and $\nu_1(\text{free NO}_3^-)$ mode of appear to incorporate at approximately the same frequency (Table 5) while the convolved $\nu(\text{C-H})$ and of $\nu(-\text{OH})$ peaks of ethylene glycol appear to be influenced by the identity of the metal substituent.

Table 5. Raman peak assignments of unsubstituted and substituted microwave synthesized α -Ni(OH)₂ nanosheet.⁴⁹

Signal Source	Peak Assignment	Experimental wavenumber (cm ⁻¹)				
		α -Ni(OH) ₂	Ni-Al ₁₀	Ni-Co ₁₀	Ni-Mn ₁₀	Ni-Zn ₁₀
α -Ni(OH) ₂ lattice	ν (E _g)	458	463	458	446	440
	ν (M(O/OH))	–	539	520	520	523
	ν (-OH stretch)	3657	3657	3657	3657	3651
Nickel-nitrate precursor	ν_1 (Free NO ₃ ⁻)	1042	1042	1040	1040	1046
Ethylene Glycol precursor	ν (C-H)	2854	2878	2844	2848	2882
Urea precursor	ν (C-N)	1173	1174	1174	1172	1174

3.5. Electrochemical Characterization

3.5.1. Analysis of 1st Cycle Galvanostatic Charge-Discharge

To evaluate how substitution affects the specific discharge capacity of α -Ni(OH)₂ a voltage vs. specific capacity plot (Figure 14) was generated from galvanostatic measurements. As discussed above, Raman spectroscopy supported the presence nitrates, urea, and ethylene glycol, while ICP analysis indicated varying concentration of substituents; however, for the purposes of this study, the specific capacity was normalized to the mass of synthesized material (α -Ni(OH)₂, Ni-Al₁₀ Ni-Co₁₀ Ni-Mn₁₀ or Ni-Zn₁₀) used during electrode fabrication. The cell was charged and discharged four times to activate the cathode material and nickel current collector, and these cycles will be referred to as formation cycles and are not included during cycling analysis, with the

5th cycle being referred to as the 1st cycle here after.^{26, 66}

For the 1st discharge cycle, all microwave synthesized nanosheet samples exhibit a voltage plateau between 1.80 V and 1.65 V without any appreciable capacity after 1.60 V. Unsubstituted α -Ni(OH)₂ had an initial discharge capacity ($239 \pm 13.3 \text{ mAh g}^{-1}_{\text{active}}$), lower than previously reported discharge capacities of base catalyzed α -Ni(OH)₂ cycled a NaOH electrolyte.⁶⁷ A number of factors may influence the discharge capacities including loading⁶⁸, cathode material differences⁶⁹, electrolyte differences,⁷⁰ cycling protocols, and ageing.⁷⁰ A prior study on the aging of α -Ni(OH)₂ into β -Ni(OH)₂ by *in situ* Raman spectroscopy indicated that when α -Ni(OH)₂ is exposed to H₂O at ambient temperatures, it began to convert to the β -polymorph resulting in a mixed α/β -Ni(OH)₂ material in as little as four days.⁷¹ It has been reported that the concentration of the electrolyte used may influence the rate of phase transformation and cycle performance of aluminum-substituted α -Ni(OH)₂ with more concentrated electrolyte solutions causing a more rapid phase transformation and capacity fade.⁷⁰ In the present study, an electrolyte formulation (6M KOH/1M LiOH) optimized for the zinc anode⁵⁰ was used and is thought to increase the aging rate of α -Ni(OH)₂ \rightarrow β -Ni(OH)₂ while in the cell. This aging likely begins during electrolyte infiltration of the electrode and continues during the formation cycles that are inherent to Ni(OH)₂ cathodes, which in this study lasts for upwards of two days. The cycling protocol used to fully evaluate the substituents effect on Ni^{2+/3+} redox and to purposefully induce OER may also contribute to lower electrochemical discharge capacities compared to previous studies by lowering charge efficiencies;^{26, 69} however the objective of this cycling regime was not cycling performance, but rather a cathodic study.

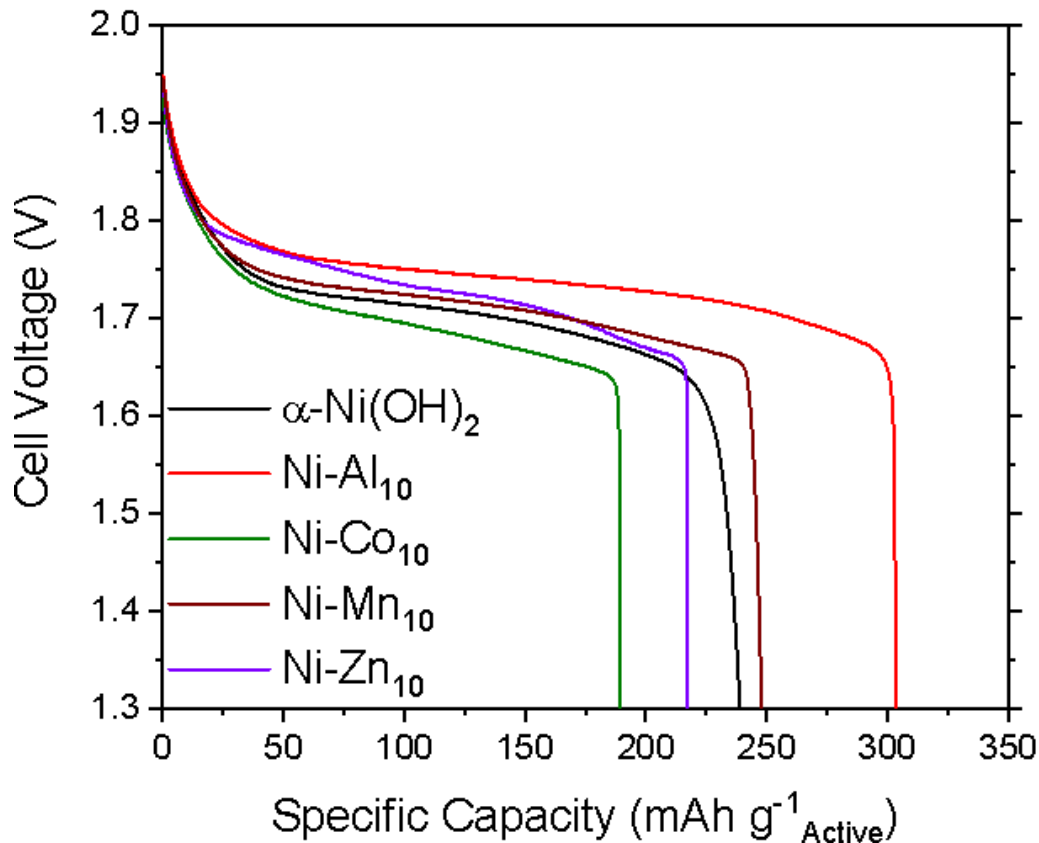


Figure 14. First cycle discharge capacity. Voltage vs. specific capacity for 1st cycle discharge of substituted and unsubstituted α -Ni(OH)₂ nanosheets at a mass normalized current of 84.4 mA·g⁻¹_{active} between 1.3-2.0 V in 6M KOH and 1 M LiOH vs 3D Zn Sponge.⁴⁹

Ni-Al₁₀ enabled a greater discharge capacity (303 ± 13 mAh g⁻¹_{active}) than unsubstituted α -Ni(OH)₂ nanosheets and shared similar discharge capacities reported in another study performed using a concentrated alkaline electrolyte, but not as high as others.^{51, 69} The increased discharge capacity associated with unsubstituted α -Ni(OH)₂ has been explained by the non-integral oxidation state of the α and γ -phases that occur because of the presence of the “free” anions and cations in the interlayer region of α -Ni(OH)₂ and γ -NiOOH⁶⁹ and interlayer anions may also influence the electron density around the nickel sites.^{26, 56} In this study, Raman spectroscopy of Ni-Al₁₀ indicated a larger relative intensity of the free nitrate mode and changes in the local potential energy

environment as a result of Al^{3+} substitution may be a factor in Ni-Al₁₀'s improved discharge capacity compared to unsubstituted α -Ni(OH)₂. The Al^{3+} content has been shown to play an important role in the electrochemical performance up to a certain concentration with the specific discharge capacity decreasing when the $[\text{Al}^{3+}]$ is greater than 10 at%.^{21, 23, 27} ICP analysis indicated that the as prepared Ni-Al₁₀ surpassed 10 at% which may influence the overall discharge capacity, but the results are comparable to other aluminum-substituted α -Ni(OH)₂ materials.^{27, 51, 69}

Ni-Co₁₀ had a significantly lower initial discharge capacity ($190 \pm 13 \text{ mAh g}^{-1}_{\text{active}}$) compared to that of unsubstituted α -Ni(OH)₂ by ~20%, which has previously been attributed to Co suppressing the oxidation of Ni^{2+} by preventing the complete α -Ni(OH)₂→ γ -NiOOH oxidation.⁷² The initial discharge capacity of Ni-Mn₁₀ ($248 \pm 13 \text{ mAh g}^{-1}_{\text{active}}$) is within the electrode-to-electrode standard deviation of unsubstituted α -Ni(OH)₂, but based on ICP analysis, had the lowest concentration of substituent incorporated into the Ni(OH)₂ framework which may help explain the similar capacities of Ni-Mn₁₀ and unsubstituted α -Ni(OH)₂. The initial discharge capacity of Ni-Zn₁₀ ($217 \pm 13 \text{ mAh g}^{-1}_{\text{Ni-Zn}}$) was ~90% of unsubstituted α -Ni(OH)₂ possibly because Ni-Zn₁₀ does not suppress oxidation in the same way as cobalt, nor does it improve the discharge capacity like Ni-Al₁₀. As discussed above, SEM micrographs of Ni-Co₁₀, Ni-Mn₁₀, and Ni-Zn₁₀ showed an increase in the aggregate size of interconnected nanosheets compared to α -Ni(OH)₂, the larger aggregate size may result in a longer diffusion path for the electrolyte ions and subsequent poor electrochemical performance,⁴⁵ and is supported by a decrease in BET surface area and pore cumulative pore volume upon substitution.

Differential capacity (dQ/dV) analysis is a common method used to evaluate the

gradual changes and failure mechanisms of Li-ion cells, whereby taking the derivative of the cell capacity with respect to voltage, dQ/dV , transposes a voltage plateau into well-defined peaks.^{66, 73, 74} In the present work, differential capacity analysis plots were generated directly from the galvanostatic cathode half-cell experiments in order to study the influence of substitution on the redox and oxygen evolution voltages of the nickel hydroxide cathodes (Figure 15a-e). Without the use of high precision dQ/dV analysis, the raw data required a line smoothing and peak fitting analysis in order to facilitate the comparison of samples.⁷⁴ The line smoothing and peak fitting analysis are overlain with the raw data of unsubstituted α -Ni(OH)₂ (Figure 15 a) for comparison.

The dQ/dV analysis of unsubstituted α -Ni(OH)₂ shows two well-defined anodic peaks (Figure 15a) as the cell is charged from 1.3 V to 2.0 V, and a single cathodic peak on the reverse sweep. Ordinarily, the first anodic peak would be assigned to oxidation of α -Ni(OH)₂→ γ -NiOOH and the single cathodic peak assigned as the reduction γ -NiOOH→ α -Ni(OH)₂.⁶⁶ The second anodic peak at the higher voltage corresponds to the parasitic oxygen evolution reaction. However, as discussed previously aging studies of α -Ni(OH)₂ in H₂O showed a mixed α/β -Ni(OH)₂ material in as little as four days.⁷¹ In the alkaline electrolyte used in this study, the α -Ni(OH)₂ material likely begins its transformation much more quickly, and assigning the anodic and cathodic peaks as purely α -Ni(OH)₂→ γ -NiOOH or γ -NiOOH→ α -Ni(OH)₂ may not be entirely accurate as it is likely a α/β -Ni(OH)₂ mixed phased material may be formed after the formation cycling process.

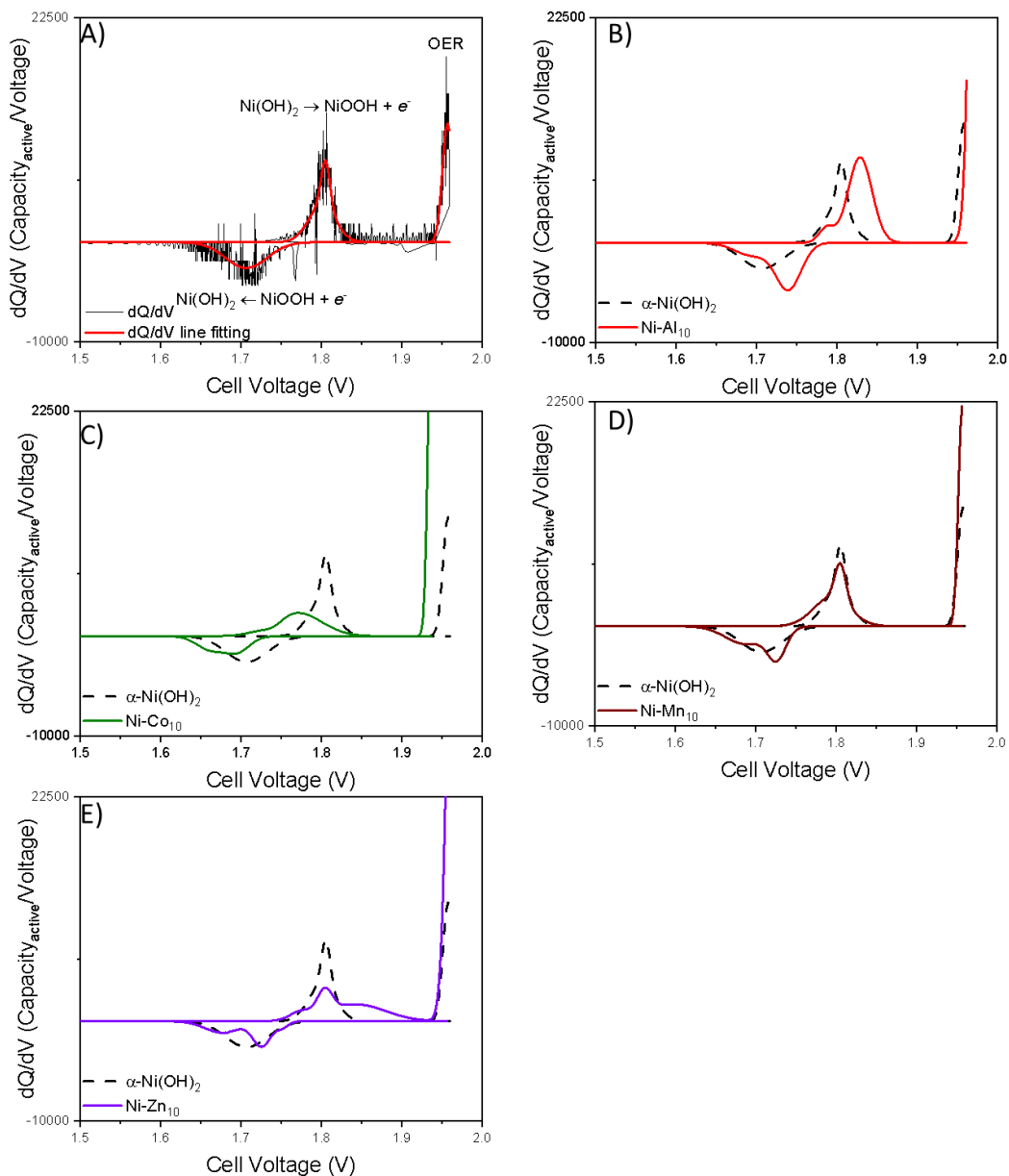


Figure 15. First cycle differential capacity (dQ/dV) analysis. (A) Differential Capacity (dQ/dV) plots of unsubstituted $\alpha\text{-Ni(OH)}_2$: a comparison of raw differential capacity data and differential capacity with a line fitting analysis. B-E) Differential capacity analysis galvanostatic charge-discharge cycle of (B) Ni-Al₁₀, (C) Ni-Co₁₀, (D) Ni-Mn₁₀, and (E) Ni-Zn₁₀, compared with unsubstituted $\alpha\text{-Ni(OH)}_2$.⁴⁹

The dQ/dV analysis of Ni-Al₁₀ (Figure 15b) is overlain with unsubstituted $\alpha\text{-Ni(OH)}_2$ to highlight the effects of Al³⁺ substitution on the redox and OER voltages of $\alpha\text{-Ni(OH)}_2$. Ni-Al₁₀ induced a shift in the anodic and cathodic peak positions (summarized in Table 6) to higher voltages corresponding to a change in local potential energy environment when

Al³⁺ substituted into the α -Ni(OH)₂ structure and is supported by changes in frequencies of the $\nu(E_g)$ lattice mode. There is the emergence of another anodic peak that is convolved with the oxidation peak of Ni-Al₁₀ indicating two unique electrochemical environments, which may indicate a mixed phase exists. Prior work has shown that Al³⁺ can leach out of the Ni(OH)₂ structure in a concentrated electrolyte⁷⁵ and this may be an Al³⁺ deficient Ni(OH)₂ oxidation or β -Ni(OH)₂ while the prominent anodic peak is the α -phase oxidation of Ni-Al₁₀; however further work is needed to confirm this interpretation. The mass-normalized anodic and cathodic peak areas of Ni-Al₁₀ have a visually larger area under the curve corresponding to the improved charge storage performance observed in Figure 14. Ni-Al₁₀ also shifted the OER voltage to more positive values offering a wider operational voltage window.

Table 6. Differential capacity analysis of cathodic voltages, anodic voltages and oxygen evolution reaction (OER) of unsubstituted α -Ni(OH)₂ and substituted nanosheets.

Material ID	Differential capacity analysis		
	Cathodic peak Voltage (V)	Anodic peak Voltage (V)	OER Voltage (V)
α -Ni(OH) ₂	1.71	1.80	1.95
Ni-Al ₁₀	1.74	1.83	1.96
Ni-Co ₁₀	1.68	1.77	1.93
Ni-Mn ₁₀	1.72	1.80	1.95
Ni-Zn ₁₀	1.72	1.81	1.95

Ni-Co₁₀ (Figure 15c) shifted the oxidation, reduction and OER peaks to lower voltages (Table 6) compared to α -Ni(OH)₂ which is consistent with previous voltammetric studies of Co substituted α -Ni(OH)₂.^{30, 31, 76} Prior work has suggested that substitution of Co²⁺ can lower the band gap increasing the conductivity of Ni-Co₁₀

relative to α -Ni(OH)₂ while locally Co(OH)₂ oxidizes forming a conductive CoOOH.⁴⁵ The mass normalized anodic and cathodic peak areas of Ni-Co₁₀ have a visually smaller area under the curve indicating its decreased charge storage potential.

The anodic and cathodic peak positions and areas of Ni-Mn₁₀ (Figure 15 d) are similar to that of α -Ni(OH)₂ (Table 6) which is not entirely unexpected with an atomic ratio of Ni_{10.97}Mn_{0.03}. Ni-Zn₁₀ (Figure 15e) exhibited a dQ/dV plot different than the other substituents evaluated as noted by the emergence of a secondary anodic and cathodic peaks. These bi-modal peaks may be related to the secondary low angle diffraction peak seen in Figure 11 and may further support the existence of a mixed phased material as discussed above.

3.5.2. Analysis of the Effect of Cycling

The effect of substitution on cycling performance of α -Ni(OH)₂ was examined for 30 charge and discharge cycles (Figure 16). The discharge capacity of α -Ni(OH)₂ initially fades within the first five cycles, stabilizing at 225 ± 13 mAh/g_{active} with negligible capacity loss thereafter. The cycling of unsubstituted α -Ni(OH)₂ nanosheets likely involves the phase transition from α -Ni(OH)₂ → β -Ni(OH)₂^{9, 18} and is supported by 1st and 30th cycle dQ/dV analysis of α -Ni(OH)₂ (discussed below).

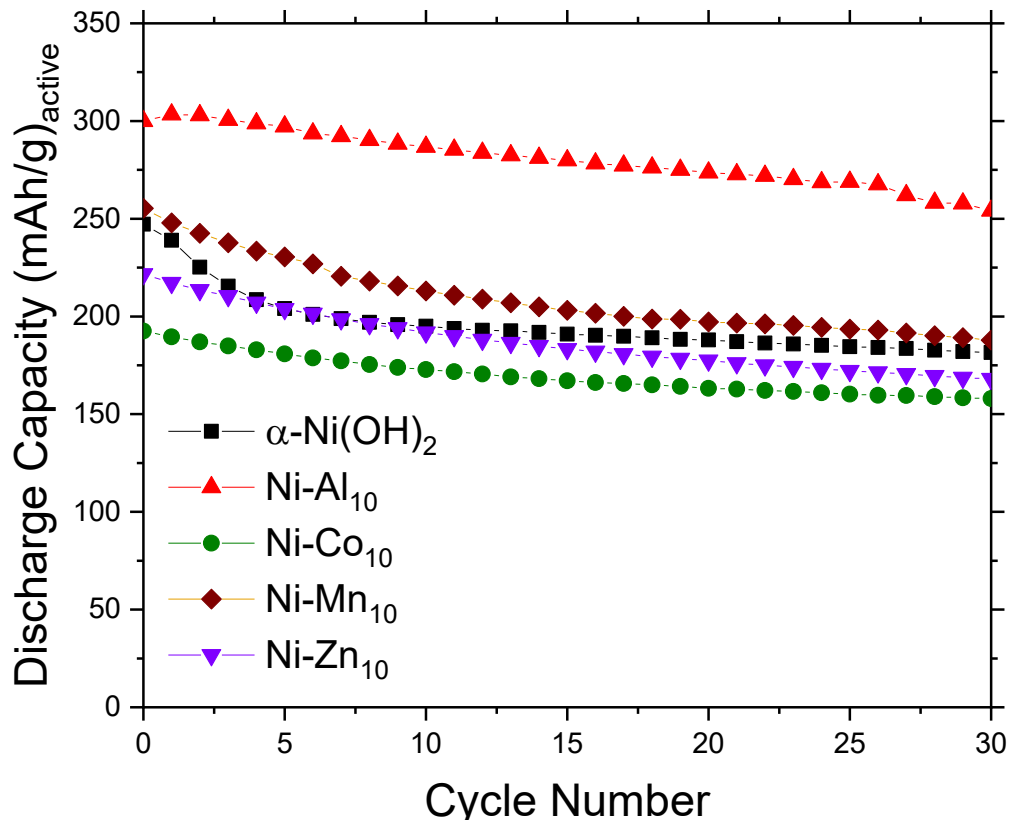


Figure 16. Effect of cycling on the discharge capacity. Analysis of the effect of cycling of substituted and unsubstituted α -Ni(OH)₂ nanosheets at a mass normalized current of $84.4 \text{ mA} \cdot \text{g}^{-1}_{\text{active}}$ between 1.3-2.0 V in 6M KOH and 1 M LiOH vs NRLs 3D Zn Sponge.⁴⁹

Ni-Al₁₀ outperforms all other materials evaluated and showed the highest overall discharge capacity for over 30 cycles without the initial capacity fade observed for with α -Ni(OH)₂. Ni-Co₁₀ has the lowest overall discharge capacity for the duration of cycling but with little appreciable capacity fade. If cobalt suppress the oxidation of Ni²⁺ by preventing the complete α -Ni(OH)₂ → γ -NiOOH oxidation⁷² then perhaps the inclusion of cobalt into the structure of α -Ni(OH)₂ increases the conversion to β -Ni(OH)₂ by limiting the complete oxidation of α -Ni(OH)₂, such that by the end of the formation cycling it is predominantly the β -polymorph. However, further work is needed to confirm this thinking. Ni-Mn₁₀ has a comparable initial discharge capacity to α -Ni(OH)₂ but fades at a lower rate than α -Ni(OH)₂ which might suggest that even at low relative atomic %, Mn²⁺

substitution into the α -Ni(OH)₂ structure slows but does not prevent the α to β phase transition.

Examining the capacity retention during cycling is a useful metric to consider when evaluating the stability of α -Ni(OH)₂ materials (Table 7). α -Ni(OH)₂ nanosheets only retained 75% of its initial capacity while Ni-Mn₁₀ (75%) or Ni-Zn₁₀ (77%) only slightly improved the capacity retention under these charging conditions. Ni-Al₁₀ and Ni-Co₁₀ both improved the capacity retention compared to unsubstituted α -Ni(OH)₂ with an 83% retention each however only Ni-Al₁₀ increased the discharge capacity.

Table 7. Electrochemical properties of unsubstituted α -Ni(OH)₂ and substituted nanosheets. *The estimated standard deviation between electrodes was ± 13 mAh/g_{active}.

Material ID	Discharge capacity (mAh/g)		Capacity Retention (%)
	1 st cycle*	30 th cycle*	
α -Ni(OH) ₂	239	180	75.3
Ni-Al ₁₀	303	252	83.2
Ni-Co ₁₀	189	157	83.1
Ni-Mn ₁₀	247	186	75.3
Ni-Zn ₁₀	217	167	77.0

The 1st and 30th cycle dQ/dV analysis of all samples were compared to evaluate the effect of substitution on cycling performance (Figure 17). α -Ni(OH)₂ (Figure 17 a) show a distinct change in redox peak positions and shape. Here, two redox peaks are observed while the OER voltage shifted to higher voltages which might indicate an increase in internal resistance of the cathode⁷⁵ or may be due to oxygen build up on the electrode as a result of inducing OER at each cycle. The 30th cycle dQ/dV redox peaks are suspected to be predominantly associated the β -polymorph with previous reports indicating that α -Ni(OH)₂ has a lower oxidation voltage than β -Ni(OH)₂.¹⁸

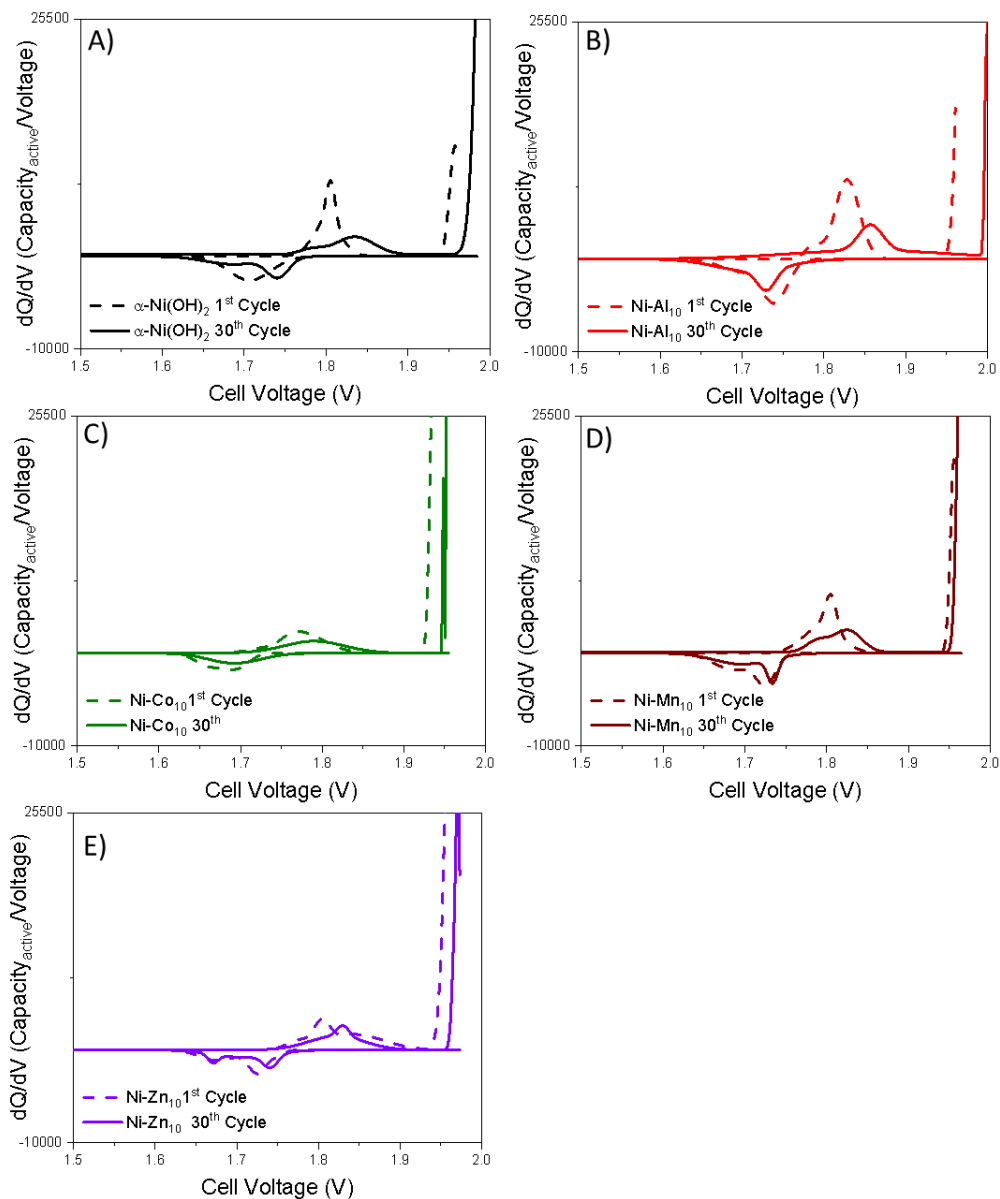


Figure 17. Effect of cycling on the differential capacity (dQ/dV). Analysis of the effect of cycling: 1st cycle and 30th cycle (dQ/dV) analysis of (A) unsubstituted α -Ni(OH)₂, (B) Ni-Al₁₀, (C) Ni-Co₁₀, (D) Ni-Mn₁₀, and (E) Ni-Zn₁₀.⁴⁹

The 1st and 30th cycle dQ/dV analysis of all metal substituted samples showed a similar separation in the redox peaks, and shift in OER voltages (Figure 17b-e). The electrochemical discharge capacity and cycling stability of Ni-Al₁₀ might indicate that Al³⁺ stabilizes the α -phase by exhibiting an increased discharge capacity and higher capacity retention over 30 cycles relative to unsubstituted α -Ni(OH)₂, but the changes in

redox peak voltages from the 1st to the 30th cycle dQ/dV analysis (Figure 17b) indicates that it may only partially suppress the α to β phase transition. Another factor that could result in the changes observed from the 1st to the 30th cycle dQ/dV analysis of Ni-Al₁₀ is aluminum leaching out of the α -Ni(OH)₂ structure causing a degradation in the overall electrochemical performance^{70, 75, 77} but further analysis is needed to determine this. Ni-Co₁₀ (Figure 17 c) remains relatively unchanged from the 1st to 30th cycles with only a gradual shift in redox and OER peaks. This further supports the idea that although the inclusion of cobalt into the α -Ni(OH)₂ structure reduces the initial Ni^{2+/3+} redox voltages, Ni-Co₁₀ did not stabilize the α -phase and may aid the transition of α to β during the formation cycles. Ni-Mn₁₀ showed a similar change in the 1st and 30th redox peaks of unsubstituted α -Ni(OH)₂ (Figure 17 d) which with a low relative at% of Mn²⁺ is not unexpected. A similar trend in Ni-Zn₁₀ (Figure 17 e) redox voltages is observed as it is cycled: the oxidation peak gradually drifts to higher voltages.

A common trend seen among the Ni(OH)₂ cathode materials is that oxidation voltages trend to higher voltages upon cycling, and will ultimately limit the long-term cycling of the cell. At a certain point, the cell will reach the upper voltage window before fully charging, which will start a process of limited return charging and depending on at what voltage oxidation takes place, the voltage shifts could influence the cell's capacity and lifetime. Substituents within α -Ni(OH)₂ therefore need to be considered based their influence on electrochemical charge storage, stability, and effect on the redox/OER voltages α -Ni(OH)₂.

4. CONCLUSIONS

Nanostructured α -Ni(OH)₂ materials with different metal-ion substituents (aluminium, cobalt, manganese, zinc) were synthesized using a rapid and scalable microwave-assisted hydrothermal synthesis technique, and the physiochemical and electrochemical properties of the materials were evaluated as cathodes for aqueous rechargeable Ni-Zn batteries. The nanosheet morphologies were maintained at an synthetic Ni-to-*M* substitution atomic ratio of 9:1 with smaller more dense nanosheet aggregates observed with Ni-Al₁₀ while Ni-Co₁₀, Ni-Mn₁₀, and Ni-Zn₁₀ produced larger nanosheet aggregates compared to unsubstituted α -Ni(OH)₂. The majority of pores for all nanosheet sample were in the mesopore (>2 nm-50 nm) and macropore range (>50 nm). Ni-Al₁₀, Ni-Co₁₀, and Ni-Mn₁₀ decreased the BET surface area while Ni-Zn₁₀ increased the surface area. ICP analysis found that Ni-Al₁₀ and Ni-Zn₁₀ had a higher experimental Ni:M ratio than the nominal synthetic ratios. Ni-Co₁₀ most closely matched the nominal synthetic Ni:M ratio, while Ni-Mn₁₀ had a lower experimental Ni:M ratio. The different atomic ratios of the surveyed substituents may be due to the differences in K_{sp} and hydrolysis and condensation kinetics of the metal hydroxides.

The overall α -Ni(OH)₂ crystal structure was preserved up to 20% atomic substitution (Ni-Zn₁₀). From X-ray diffraction patterns, Ni-Al₁₀ had a larger interlayer spacing, and Ni-Zn₁₀ showed a new low angle peak supporting a mixed phase Ni-Zn cathode material. the lack of additional XRD peaks that would indicate the substituted metal ions were within a separate phase and the presence of new M-O modes observed by Raman spectroscopy supports that the Al, Co and Mn substituents are at least partially located

within the Ni(OH)₂ lattice. Vibrational modes of nitrate, ethylene glycol, and urea modes were also identified indicating the coordination of the precursor materials to α -Ni(OH)₂.

The metal ion-substituted α -Ni(OH)₂ nanosheets were tested as cathodes within composite electrodes at relevant mass loadings vs. Zn-sponge anodes. Differential capacity analysis revealed that the substituents resulted in substantial shifts of the Ni^{2+/3+} redox peaks and the onset potential for oxygen evolution. The differential capacity analysis showed that compared with unsubstituted α -Ni(OH)₂, Ni-Al₁₀ resulted in increasing the redox and OER voltages, while Ni-Co₁₀ had the opposite effect of lowering the redox and OER voltages of α -Ni(OH)₂. Ni-Al₁₀ nanosheets also provided substantially higher capacities compared with other samples prepared using other divalent cations. The discharge of Ni-Al₁₀ capacity remained higher than other samples with cycling, but changes in the oxidation voltage of dQ/dV analysis may indicate the formation of β -Ni(OH)₂. Ni-Al₁₀ and Ni-Co₁₀ improved the capacity retention compared to unsubstituted α -Ni(OH)₂. The nature and influence of metal substitution into α -Ni(OH)₂ using a rapid and scalable microwave-assisted hydrothermal synthesis technique provides insight into the development and design criteria of α -Ni(OH)₂ cathodes that are needed for next generation Ni-Zn batteries.

REFERENCES

1. Yang, Y.; Bremner, S.; Menictas, C.; Kay, M., Battery energy storage system size determination in renewable energy systems: A review. *Renewable and Sustainable Energy Reviews* **2018**, *91*, 109-125.
2. Li, Y.; Dai, H., Recent advances in zinc-air batteries. *Chem Soc Rev* **2014**, *43* (15), 5257-75.
3. Zhu, J.; Wierzbicki, T.; Li, W., A review of safety-focused mechanical modeling of commercial lithium-ion batteries. *Journal of Power Sources* **2018**, *378*, 153-168.
4. Cooper, A., Dreamliners grounded globally due to fire risk. *CNN* 2013.
5. Plummer, L., Own a Galaxy Note 7 Samsung is now replacing handsets in the U.K. after fears faulty devices could explode. *Daily Mail* 2016.
6. Parker, J. F.; Chervin, C. N.; Pala, I. R.; Machler, M.; Burz, M. F.; Long, J. W.; Rolison, D. R., Rechargeable nickel–3D zinc batteries: An energy-dense, safer alternative to lithium-ion. *Science* **2017**, *356* (6336), 415-418.
7. Lebeau, P., Electric car blaze raises questions for Tesla. *NBC NEWS* **2013**.
8. Santhanagopalan, S., Kim, Gi-Heon, Keyers, Matthew, Pesaran, Ahmad, Smith, Kandler, Neubauer, Jeremy, *Design and Analysis of Large Lithium-Ion Battery Systems*. Artech House. 2015: Boston, 2015.
9. Huang, M.; Li, M.; Niu, C.; Li, Q.; Mai, L., Recent Advances in Rational Electrode Designs for High-Performance Alkaline Rechargeable Batteries. *Advanced Functional Materials* **2019**.
10. Beard, K. W., *Linden's Handbook of Batteries, Fifth Edition*. McGraw-Hill Education: New York, Chicago, San Francisco, Athens, London, Madrid, Mexico City, Milan, New Delhi, Singapore, Sydney, Toronto, 2019.
11. Parker, J. F.; Chervin, C. N.; Nelson, E. S.; Rolison, D. R.; Long, J. W., Wiring zinc in three dimensions re-writes battery performance—dendrite-free cycling. *Energy Environ. Sci.* **2014**, *7* (3), 1117-1124.
12. Parker, J. F.; Nelson, E. S.; Wattendorf, M. D.; Chervin, C. N.; Long, J. W.; Rolison, D. R., Retaining the 3D framework of zinc sponge anodes upon deep discharge in Zn-air cells. *ACS Appl Mater Interfaces* **2014**, *6* (22), 19471-6.
13. Ko, J. S.; Geltmacher, A. B.; Hopkins, B. J.; Rolison, D. R.; Long, J. W.; Parker, J. F., Robust 3D Zn Sponges Enable High-Power, Energy-Dense Alkaline Batteries. *ACS Applied Energy Materials* **2018**, *2* (1), 212-216.

14. Hopkins, B. J.; Sassin, M. B.; Chervin, C. N.; DeSario, P. A.; Parker, J. F.; Long, J. W.; Rolison, D. R., Fabricating architected zinc electrodes with unprecedented volumetric capacity in rechargeable alkaline cells. *Energy Storage Materials* **2020**, *27*, 370-376.
15. Hall, D. S.; Lockwood, D. J.; Bock, C.; MacDougall, B. R., Nickel hydroxides and related materials: a review of their structures, synthesis and properties. *Proc Math Phys Eng Sci* **2015**, *471* (2174), 20140792.
16. K. I. Pandya, W. E. O. G., D. A. Corrigan, J. McBreen, and R. W. Hoffman, Extended x-ray absorption fine structure investigations of nickel hydroxides. *The Journal of Physical Chemistry* **1990**, *94* (1), 21-26.
17. Li, J.; Shangguan, E.; Guo, D.; Tian, M.; Wang, Y.; Li, Q.; Chang, Z.; Yuan, X.-Z.; Wang, H., Synthesis, characterization and electrochemical performance of high-density aluminum substituted α -nickel hydroxide cathode material for nickel-based rechargeable batteries. *Journal of Power Sources* **2014**, *270*, 121-130.
18. Miao, Y.; Ouyang, L.; Zhou, S.; Xu, L.; Yang, Z.; Xiao, M.; Ouyang, R., Electrocatalysis and electroanalysis of nickel, its oxides, hydroxides and oxyhydroxides toward small molecules. *Biosens Bioelectron* **2014**, *53*, 428-39.
19. Nie, Y. J.; Yang, H. X.; Pan, J. Q.; Li, W.; Sun, Y. Z.; Niu, H. X., Synthesis of nano-Ni(OH)₂/porous carbon composite as superior cathode materials for alkaline power batteries. *Electrochimica Acta* **2017**, *252*, 558-567.
20. Ash, B.; Kheti, J.; Sanjay, K.; Subbaiah, T.; Anand, S.; Paramguru, R. K., Physico-chemical and electro-chemical properties of nickel hydroxide precipitated in the presence of metal additives. *Hydrometallurgy* **2006**, *84* (3-4), 250-255.
21. Yao, J.; Li, Y.; Li, Y.; Zhu, Y.; Wang, H., Enhanced cycling performance of Al-substituted α -nickel hydroxide by coating with β -nickel hydroxide. *Journal of Power Sources* **2013**, *224*, 236-240.
22. Zhao, Y., Al-substituted α -nickel hydroxide prepared by homogeneous precipitation method with urea. *International Journal of Hydrogen Energy* **2004**, *29* (8), 889-896.
23. L. J. Yang, X. P. G., Q. D. Wu, H. Y. Zhu, and G. L. Pan, Phase Distribution and Electrochemical Properties of Al-Substituted Nickel Hydroxides. *The Journal of Physical Chemistry C* **2007**, *111* (12), 4614-4619.
24. Zhao, Y. L.; Wang, J. M.; Chen, H.; Pan, T.; Zhang, J. Q.; Cao, C. N., Different additives-substituted α -nickel hydroxide prepared by urea decomposition. *Electrochimica Acta* **2004**, *50* (1), 91-98.

25. Mavis, B.; Akinc, M., Three-component layer double hydroxides by urea precipitation: structural stability and electrochemistry. *Journal of Power Sources* **2004**, *134* (2), 308-317.
26. Li, Y. W.; Yao, J. H.; Liu, C. J.; Zhao, W. M.; Deng, W. X.; Zhong, S. K., Effect of interlayer anions on the electrochemical performance of Al-substituted α -type nickel hydroxide electrodes. *International Journal of Hydrogen Energy* **2010**, *35* (6), 2539-2545.
27. Nore'us, W.-K. H. a. D., Alpha Nickel Hydroxides as Lightweight Nickel Electrode Materials for Alkaline Rechargeable Cells. *Chemistry of Materials* **2003**, *15*, 974-978.
28. Liu Bing, Y. H., Zhang Yunshi, Zhou Zuoxiang, Song Deying, Cyclic voltammetric studies of stabilized α -nickel hydroxide electrode. *Journal of Power Sources* **1999**, *79*, 277-280.
29. Ortiz, M. G.; Castro, E. B.; y Real, S. G., The cobalt content effect on the electrochemical behavior of nickel hydroxide electrodes. *International Journal of Hydrogen Energy* **2012**, *37* (13), 10365-10370.
30. Armstrong, R. D.; Briggs, G. W. D.; Charles, E. A., Some effects of the addition of cobalt to the nickel hydroxide electrode. *Journal of Applied Electrochemistry* **1988**, *18*, 215.
31. Bendert, D. A. C. a. R. M., Effect of Coprecipitated Metal Ions on the Electrochemistry of Nickel Hydroxide Thin Films: Cyclic Voltammetry in 1M KOH. *Journal of The Electrochemical Society* **1989**, *136* (3), 723-728.
32. Bao, J.; Zhu, Y.; Zhang, Z.; Xu, Q.; Zhao, W.; Chen, J.; Zhang, W.; Han, Q., Structure and electrochemical properties of nanometer Cu substituted α -nickel hydroxide. *Materials Research Bulletin* **2013**, *48* (2), 422-428.
33. R.S. Jayashree., P. V. K., Layered double hydroxides of Ni with Cr and Mn as candidateelectrode materials for alkaline secondary cells. *Journal of Power Sources* **2002**, *107*, 120-124.
34. Morishita, M.; Ochiai, S.; Kakeya, T.; Ozaki, T.; Kawabe, Y.; Watada, M.; Tanase, S.; Sakai, T., Structural Analysis by Synchrotron XRD and XAFS for Manganese-Substituted α - and β -Type Nickel Hydroxide Electrode. *Journal of The Electrochemical Society* **2008**, *155* (12).
35. Tessier, C.; Guerlou-Demourgues, L.; Faure, C.; Demourgues, A.; Delmas, C., Structural study of zinc-substituted nickel hydroxides. *Journal of Materials Chemistry* **2000**, *10* (5), 1185-1193.

36. Tessier, C.; Faure, C.; Guerlou-Demourgues, L.; Denage, C.; Nabias, G.; Delmas, C., Electrochemical Study of Zinc-Substituted Nickel Hydroxide. *Journal of The Electrochemical Society* **2002**, *149* (9), A1136-A1145.
37. Huang, H.; Guo, Y.; Cheng, Y., Ultrastable α phase nickel hydroxide as energy storage materials for alkaline secondary batteries. *Applied Surface Science* **2018**, *435*, 635-640.
38. Cochran, E. A.; Woods, K. N.; Johnson, D. W.; Page, C. J.; Boettcher, S. W., Unique chemistries of metal-nitrate precursors to form metal-oxide thin films from solution: materials for electronic and energy applications. *Journal of Materials Chemistry A* **2019**, *7* (42), 24124-24149.
39. Bilecka, I.; Niederberger, M., Microwave chemistry for inorganic nanomaterials synthesis. *Nanoscale* **2010**, *2* (8).
40. Faraji, S.; Ani, F. N., Microwave-assisted synthesis of metal oxide/hydroxide composite electrodes for high power supercapacitors – A review. *Journal of Power Sources* **2014**, *263*, 338-360.
41. Zhang, X.; Li, C.; Miao, W.; Sun, X. Z.; Wang, K.; Ma, Y. W., Microwave-assisted synthesis of 3D flowerlike α -Ni(OH)₂ nanostructures for supercapacitor application. *Sci. China-Technol. Sci.* **2015**, *58* (11), 1871-1876.
42. Zhu, Y.; Cao, C.; Tao, S.; Chu, W.; Wu, Z.; Li, Y., Ultrathin nickel hydroxide and oxide nanosheets: synthesis, characterizations and excellent supercapacitor performances. *Sci Rep* **2014**, *4*, 5787.
43. Lamiel, C.; Nguyen, V. H.; Kumar, D. R.; Shim, J.-J., Microwave-assisted binder-free synthesis of 3D Ni-Co-Mn oxide nanoflakes@Ni foam electrode for supercapacitor applications. *Chemical Engineering Journal* **2017**, *316*, 1091-1102.
44. Benito, P.; Labajos, F. M.; Rives, V., Microwave-treated layered double hydroxides containing Ni and Al: The effect of added Zn. *Journal of Solid State Chemistry* **2006**, *179* (12), 3784-3797.
45. Li, J.; Wei, M.; Chu, W.; Wang, N., High-stable α -phase NiCo double hydroxide microspheres via microwave synthesis for supercapacitor electrode materials. *Chemical Engineering Journal* **2017**, *316*, 277-287.
46. Tao, Y.; Haiyan, Z.; Ruiyi, L.; Zaijun, L.; Junkang, L.; Guangli, W.; Zhiquo, G., Microwave synthesis of nickel/cobalt double hydroxide ultrathin flowerclusters with three-dimensional structures for high-performance supercapacitors. *Electrochimica Acta* **2013**, *111*, 71-79.

47. Godínez-Salomón, F.; Albiter, L.; Alia, S. M.; Pivovar, B. S.; Camacho-Forero, L. E.; Balbuena, P. B.; Mendoza-Cruz, R.; Arellano-Jimenez, M. J.; Rhodes, C. P., Self-Supported Hydrous Iridium–Nickel Oxide Two-Dimensional Nanoframes for High Activity Oxygen Evolution Electrocatalysts. *ACS Catalysis* **2018**, *8* (11), 10498-10520.
48. Godínez-Salomon, F.; Mendoza-Cruz, R.; Arellano-Jimenez, M. J.; Jose-Yacamán, M.; Rhodes, C. P., Metallic Two-Dimensional Nanoframes: Unsupported Hierarchical Nickel-Platinum Alloy Nanoarchitectures with Enhanced Electrochemical Oxygen Reduction Activity and Stability. *ACS Appl Mater Interfaces* **2017**, *9* (22), 18660-18674.
49. Kimmel, S. W., Hopkins, B.J., Chervin, C.N., Parker, J.F., Long, J.W., Rolison, D.R., Rhodes, C.P., Microwave Assisted Metal Substitution within Nanostructured Nickel Hydroxides for Aqueous Rechargeable Nickel–Zinc Batteries. *Manuscript in preparation*.
50. Parker, J. F.; Pala, I. R.; Chervin, C. N.; Long, J. W.; Rolison, D. R., Minimizing Shape Change at Zn Sponge Anodes in Rechargeable Ni–Zn Cells: Impact of Electrolyte Formulation. *Journal of The Electrochemical Society* **2015**, *163* (3), A351-A355.
51. Miao, C.; Zhu, Y.; Huang, L.; Zhao, T., The relationship between structural stability and electrochemical performance of multi-element doped alpha nickel hydroxide. *Journal of Power Sources* **2015**, *274*, 186-193.
52. Rolison, D. R., Catalytic Nanoarchitectures--the Importance of Nothing and the Unimportance of Periodicity. *Science* **2003**, *299* (5613), 1698-1701.
53. Zhang, Z. J.; Zhu, Y. J.; Bao, J.; Lin, X. R.; Zheng, H. Z., Electrochemical performance of multi-element doped α -nickel hydroxide prepared by supersonic coprecipitation method. *Journal of Alloys and Compounds* **2011**, *509* (25), 7034-7037.
54. Mridula Dixit, P. V. K., and J. Gopalakrishnan, Zinc-Substituted α -Nickel Hydroxide as an Electrode Material for Alkaline Secondary Cells. *Journal of The Electrochemical Society* **1999**, *146* (1), 79-82.
55. Kundu, D.; Adams, B. D.; Duffort, V.; Vajargah, S. H.; Nazar, L. F., A high-capacity and long-life aqueous rechargeable zinc battery using a metal oxide intercalation cathode. *Nature Energy* **2016**, *1* (10).
56. Chen, D.; Xiong, X.; Zhao, B.; Mahmoud, M. A.; El-Sayed, M. A.; Liu, M., Probing Structural Evolution and Charge Storage Mechanism of Ni(OH)₂ x Electrode Materials using In Operando Resonance Raman Spectroscopy. *Adv Sci (Weinh)* **2016**, *3* (6), 1500433.
57. Hall, D. S.; Lockwood, D. J.; Poirier, S.; Bock, C.; MacDougall, B. R., Raman and infrared spectroscopy of alpha and beta phases of thin nickel hydroxide films electrochemically formed on nickel. *J Phys Chem A* **2012**, *116* (25), 6771-84.

58. Sawodny, W.; Niedenzu, K.; Dawson, J. W., The vibrational spectrum of ethylene glycol. *Spectrochimica Acta Part A: Molecular Spectroscopy* **1967**, *23* (4).
59. B. Rousseau, R. K., H.O. Dessey, H.J. Geise, C. Van Alsenoy, Solids modeled by ab-initio crystal field methods. Effects of intermolecular interactions on the vibrational spectrum of urea. *Chemical Physics Letters* **1999**, *302*.
60. Wang, C.; Zhang, X.; Xu, Z.; Sun, X.; Ma, Y., Ethylene Glycol Intercalated Cobalt/Nickel Layered Double Hydroxide Nanosheet Assemblies with Ultrahigh Specific Capacitance: Structural Design and Green Synthesis for Advanced Electrochemical Storage. *ACS Appl Mater Interfaces* **2015**, *7* (35), 19601-10.
61. Breitingera, D. K.; Mohra, J.; Colognesib, D.; Parkerb, S. F.; Schukowc, H.; Schwabc, R. G., Vibrational spectra of augelites $\text{Al}_2(\text{OH})_3\text{XO}_4\text{X P, As, V}$. *Journal of Molecular Structure* **2001**.
62. Shieh, S. R.; Duffy, T. S., Raman spectroscopy of $\text{Co}(\text{OH})_2$ at high pressures: Implications for amorphization and hydrogen repulsion. *Physical Review B* **2002**, *66* (13).
63. Julien, C., Raman spectra of birnessite manganese dioxides. *Solid State Ionics* **2003**, *159* (3-4), 345-356.
64. Awan, S. U.; Hasanain, S. K.; Rashid, J.; Hussain, S.; Shah, S. A.; Hussain, M. Z.; Rafique, M.; Aftab, M.; Khan, R., Structural, optical, electronic and magnetic properties of multiphase $\text{ZnO}/\text{Zn}(\text{OH})_2/\text{ZnO}$ nanocomposites and hexagonal prism shaped ZnO nanoparticles synthesized by pulse laser ablation in Heptanes. *Materials Chemistry and Physics* **2018**, *211*, 510-521.
65. Cuscó, R.; Alarcón-Lladó, E.; Ibáñez, J.; Artús, L.; Jiménez, J.; Wang, B.; Callahan, M. J., Temperature dependence of Raman scattering in ZnO. *Physical Review B* **2007**, *75* (16).
66. Bonnicks, P.; Dahn, J. R., A Simple Coin Cell Design for Testing Rechargeable Zinc-Air or Alkaline Battery Systems. *Journal of The Electrochemical Society* **2012**, *159* (7), A981-A989.
67. Liu, C.; Li, Y., Synthesis and characterization of amorphous α -nickel hydroxide. *Journal of Alloys and Compounds* **2009**, *478* (1-2), 415-418.
68. Brisse, A. L.; Stevens, P.; Toussaint, G.; Crosnier, O.; Brousse, T., Ni(OH)₂ and NiO Based Composites: Battery Type Electrode Materials for Hybrid Supercapacitor Devices. *Materials (Basel)* **2018**, *11* (7).
69. Young, K.-H.; Wang, L.; Yan, S.; Liao, X.; Meng, T.; Shen, H.; Mays, W., Fabrications of High-Capacity α -Ni(OH)₂. *Batteries* **2017**, *3* (4).

70. Hu, M.; Yang, Z.; Lei, L.; Sun, Y., Structural transformation and its effects on the electrochemical performances of a layered double hydroxide. *Journal of Power Sources* **2011**, *196* (3), 1569-1577.
71. Hall, D. S.; Lockwood, D. J.; Poirier, S.; Bock, C.; MacDougall, B. R., Applications of in situ Raman spectroscopy for identifying nickel hydroxide materials and surface layers during chemical aging. *ACS Appl Mater Interfaces* **2014**, *6* (5), 3141-9.
72. Gong, M.; Li, Y.; Zhang, H.; Zhang, B.; Zhou, W.; Feng, J.; Wang, H.; Liang, Y.; Fan, Z.; Liu, J.; Dai, H., Ultrafast high-capacity NiZn battery with NiAlCo-layered double hydroxide. *Energy & Environmental Science* **2014**, *7* (6).
73. Smith, A. J.; Dahn, J. R., Delta Differential Capacity Analysis. *Journal of The Electrochemical Society* **2012**, *159* (3), A290-A293.
74. Smith, A. J.; Burns, J. C.; Dahn, J. R., High-Precision Differential Capacity Analysis of LiMn₂O₄/graphite Cells. *Electrochemical and Solid-State Letters* **2011**, *14* (4).
75. Morishita, M.; Kakeya, T.; Ochiai, S.; Ozaki, T.; Kawabe, Y.; Watada, M.; Sakai, T., Structural analysis by synchrotron X-ray diffraction, X-ray absorption fine structure and transmission electron microscopy for aluminum-substituted α -type nickel hydroxide electrode. *Journal of Power Sources* **2009**, *193* (2), 871-877.
76. Vidotti, M.; Salvador, R. P.; Ponzio, E. A.; Córdoba de Torresi, S. I., Mixed Ni/Co Hydroxide Nanoparticles Synthesized by Sonochemical Method. *Journal of Nanoscience and Nanotechnology* **2007**, *7* (9), 3221-3226.
77. Bardé, F.; Palacín, M. R.; Beaudoin, B.; Christian, P. A.; Tarascon, J. M., Cationic substitution in γ -type nickel (oxi)hydroxides as a means to prevent self-discharge in Ni/Zn primary batteries. *Journal of Power Sources* **2006**, *160* (1), 733-743.